A Computational Protocol for Spray Flows

Using the Quadratic Formula as the Primary Atomization Module

by

Benjamin Greenlee

A Thesis Presented in Partial Fulfillment
of the Requirements for the Degree
Master of Science

Approved April 2020 by the
Graduate Supervisory Committee:

Taewoo Lee, Chair
Marcus Herrmann
Mohamed Kasbaoui

ARIZONA STATE UNIVERSITY

May 2020

ABSTRACT

Computability of spray flows is an important issue, from both fundamental and practical perspectives. Spray flows have important applications in fuel injection, agriculture, medical devices, and industrial processes such as spray cooling. For this reason, many efforts have been devoted to experimental, computational and some theoretical aspects of spray flows. In particular, primary atomization, the process of bulk liquid transitioning to small droplets, is a central and probably the most difficult aspect of spray flows. This thesis discusses developed methods, results, and needed improvements in the modeling of primary atomization using a predictive Sauter Mean Diameter (SMD) formula. Primary atomization for round injectors and simplex atomizers is modeled using a three-step procedure. For each spray geometry, a volume-of-fluid simulation is run to resolve the trajectory of the intact liquid core. Atomization criterion is applied to the volume-of-fluid velocity field to determine atomization sites. Local droplet size is predicted at the atomization sites using the quadratic formula for Sauter Mean Diameter. Droplets with the computed drop size are injected from the atomization sites and are tracked as point-particles. A User Defined Memory (UDM) code is employed to compute steady-state Sauter Mean Diameter statistics at locations corresponding to experimental interrogation locations. The resulting Sauter Mean Diameter, droplet trajectory, and droplet velocity are compared against experimental data to validate the computational protocol. This protocol can be implemented on coarse-grid, time-averaged simulations of spray flows, and produces convincing results when compared with experimental data for pressure-atomized sprays with and without swirl. This approach is general and can be adapted in any spray geometry for complete and efficient computations of spray flows.

TABLE OF CONTENTS

CHAPTER Page

APPENDIX Page

LIST OF TABLES

Table Page

LIST OF FIGURES

Figure Page

Figure Page

Figure Page

Figure Page

Chapter 1

INTRODUCTION

Previous methods, such as the Kelvin Helmholtz-Rayleigh Taylor (KH-RT) method, have been used to estimate the break-up and atomization of straight flows, especially for flows under diesel conditions (Beale and Reitz (1999)). The main concern with these types of codes, such as the KIVA solver family, is that the simulation assumes 'blobs' of liquid are entering the domain from the inlet and then are progressively atomizing up to the break-up region. However, it is well known that for straight atomizing jets, there is an all-liquid core penetrating into a quiescent media until its ultimate atomization at the break-up length. This break-up length is roughly 100 to 150 diameters downstream for turbulent straight jets (Ruff *et al.* (1991)). Similarly, for swirling flows, thin sheets of liquid exit the injector before atomizing a short distance past the injector. The Eulerian-Lagrangian Spray Atomization method (ELSA) simulates a realistic liquid core for straight jets (Saeedipour *et al.* (2016)). The computational grid is refined well enough that the shearing of liquid parcels from the surface of the liquid column occurs. The parcels of fuel are converted into Lagrangian point-particles, with a diameter that is proportional to the local Taylor micro-scale. This method is more physically accurate than the KH-RT model; however, the grid size statistics will heavily influence the local Taylor micro-scale values, and thus the Lagrangian point-particle size. Therefore, by applying physical break-up criterion to an all liquid simulation of straight and swirling type flows, and sequentially predicting the drop size using the quadratic formula at the break-up locations, a more accurate representation and computationally inexpensive model of the primary atomization process for a multitude of spray geometries can be captured.

Chapter 2

LITERATURE REVIEW

2.1 Kelvin Helmholtz-Rayleigh Taylor Atomization Model

Beale and Reitz (1999) created a method to model spray atomization by combining the Kelvin-Helmholtz and Rayleigh-Taylor instability theorems. Kelvin-Helmholtz instability is used to model the break-up of large 'blobs' of liquid exiting the injector nozzle. The Kelvin-Helmholtz instability theorem states the break-up of the larger blobs of liquid is primarily a function of the Weber number. The Rayleigh-Taylor model was used to simulate the breakup of the larger blobs and small droplets of liquid past the break-up point of the liquid column. Peripheral atomization of the liquid column before the break-up point is also modeled by the Rayleigh-Taylor model, but with a modification in the break-up time calculation. The break-up time in the Rayleigh-Taylor model is defined as:

$$t_{RT} = \frac{C_t}{\Omega_{RT}} \tag{2.1}$$

In Equation (2.1), C_t is a constant set to 9 before the break-up point and one after the point of break-up for a diesel spray. The term Ω_{RT} is the frequency of the fastest growing wave on the surface of a given droplet. This the fastest growing wave frequency is a function of the particle acceleration, the acceleration due to gravity, and the ratio of the fluid and gas densities. Similarly, the Rayleigh-Taylor model treats the break-up of the drops as a function of the fluid acceleration and the effect of gravity. Rosin-Rammler drop size distribution model is used to estimate the distribution of drop sizes upon parcel break-up.

A model constant of 3.5 is used in both the before and after break-up regions. The break-up region of the liquid column is set in space using the Levich break-up length theory.

While this method properly models the break-up mechanisms of primary atomization, the primary issue with the KH-RT break-up model is the assumption that the liquid exits the domain in 'blobs' of liquid, rather than as an intact core as observed experimentally. Additionally, a plethora of experimentally defined modelling constants are used in this code, diminishing the predictive power of the method (i.e. the break-up time modeling coefficient C_t).

2.2 Eulerian-Lagrangian Spray Atomization Model

Saeedipour *et al.* (2016) created a hybrid modeling scheme to simulate the primary atomization process. This model relies on gathered direct numerical simulation (DNS) data of the liquid-gas interface. It uses a combined Eulerian-Lagrangian solving method. Since atomization marks an increase in surface area and a decrease in surface density, a surface density function is introduced to track the liquid-gas interface and predict when atomization occurs.

$$\tilde{\Omega} = \frac{\overline{\Sigma}}{\overline{\rho}'} \tag{2.2}$$

The surface density function (Equation (2.2)) defines the liquid-gas interface per unit mass. This density function is implemented into the conservation of momentum equation to solve the interface velocity. A source term is implemented in the formulation to account for physical atomization process and is given as:

$$S = \frac{\tilde{\Omega}\overline{\rho}'}{\tau}\left(1 - \frac{\tilde{\Omega}}{\tilde{\Omega}_{eq}}\right) \tag{2.3}$$

where τ is the time period of the interface in which the surface density reaches the equilibrium value of $\tilde{\Omega}_{eq}$.

Not only does the source term rely on these parameters, estimated from DNS simulations, it also relies on the current surface density function value. Numerical solution of this is easy, but the error will likely be high. Thus, it's hypothesized this is the reason the current results were computed using the Reynolds Averaged viscous model, to mitigate large errors through momentum field and turbulence averaging.

Spray geometries that have not been simulated by DNS cannot be simulated using this approach. Another concern of this approach is how the drop size is determined. It appears that this method only accurately computes the liquid-gas interface for previous DNS spray geometries but does not specify how the drops form and assumes the produced drop size to be proportional to the local Taylor micro-scale.

2.3 Sheet Break-up Model

Qin *et al.* (2018) derived a theoretical SMD formula for planar, air-blast assisted, liquid sheets. A similar method to Beale and Reitz (1999) KH-RT was implemented, with a few major differences. Beale and Reitz (1999) assumed that one of the major sources of liquid column and sheet instability was the surface tension between the liquid and air. Qin *et al.* (2018) assumes that the surface tension in fact leads to the creation of small droplets from the streamwise ligaments found in the high-speed planar liquid sheet being investigated. Therefore, the surface tension is regarded as a source of droplet creation rather than intact core instability. This is in part due to the high relative velocity between the gas and liquid phases, with gas having the higher velocity. Like the previous KH-RT model, initial separation of the intact liquid sheet is generated by the Kelvin-Helmholtz instability, where surface waves begin to shear from the liquid sheet as the amplitude of the waves converge on a critical value.

Linear stability analysis was conducted on a dispersion relation to determine which terms are most likely responsible for the creation of the surface waves leading to initial break-up. When calculating the disturbance growth rate, it was found that the second and fourth order terms for viscosity could be omitted as the effects of viscosity were highly outweighed by the effects of the wave number, surface tension, and density ratio. Under the assumption, found through experimental data, that short waves will generally be responsible atomization. Thus, the effect of wave number could also be omitted. When comparing this simplified dispersion relation to the full relation, good agreement was found. However, this is only for liquid sheets with high gas velocity relative to the liquid velocity.

The team then investigated the effects of gas compressibility and viscosity. Since the formulation of the SMD accounts for both sides of the symmetric planar sheet, the effects of gas compressibility and viscosity will not affect the end SMD value. The initial drop break-up, dictated by KH instability, will be heavily influenced by the gas viscosity and compressibility. Since the secondary break-up, dictated by RT instability, is largely independent of these effects, the final drop size will be the same in inviscid, incompressible gas as viscid, compressible gas. However, these properties of gas will cause discrepancies in the temporal and spatial spreading of the drops.

Much like the Rayleigh-Taylor wavenumber derived by Beale and Reitz (1999), the RT wavelength in this model is a function of the acceleration of the liquid sheet, the liquid density, and the surface tension. The final drop size is considered proportional to the RT wavelength. The SMD is then calculated by integrating over the wavelength and real part of the growth rate of the waves. A coefficient of proportionality and mass flow rate ratio are also included in this formulation. The coefficient of proportionality depends on fluid properties and injector geometry. This value is found by comparing the calculated SMD to that measured experimentally.

The spatial coordinate in which the RT instability begins to dictate drop size is estimated as where the liquid sheet begins where streamwise ligaments formed by KH instability arise. In the computations presented in the paper, this value was estimated as the break-up length, which was selected based on past experimental results.

While this formula does generate SMD values close to experimental results, it is only applicable to liquid sheets under specific operating conditions. While this is extremely useful in the cases of high gas velocity, this formulation cannot be applied to liquid sheets with coaxial gas streams with velocities roughly below 60 m/s. Using the complete dispersion relation may lead to a more broad formulation; however, the complexity of the computation would increase drastically. The selection of equation constants would also become more difficult.

Chapter 3

THE QUADRATIC FORMULA

3.1 Straight and Swirling Jets

When considering the control volume of a straight spray, logically, the volumetric flow rate at the inlet must equate to the volumetric flow rate at the exit of the control volume. This logic is used to apply the continuity and conservation of energy equations in a manner that accounts for the momentum and energy contributions of all droplets in a spray (Lee and Robinson (2010)).

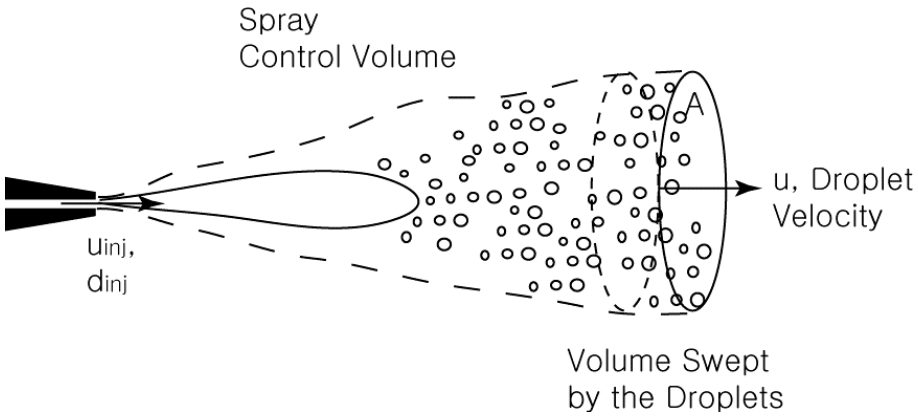

Figure 3.1: A straight spray control volume for applying the integral form of the conservation equations during spray atomization. Retrieved from Lee and Robinson (2010).

This control volume spans from the injector inlet to the region in which the entire spray has been atomized, seen in Figure 3.1. From this control volume, the continuity and energy conservation equations can be written as:

$$\rho_L u_{inj} A_{inj} = \int_{u=0}^{u_{max}} \int_{D=0}^{D_{max}} n\bar{p}(D,u)\frac{\pi D^3}{6}\rho_L u A dD du \approx \frac{\pi}{6} n \rho_L u_L A \sum_{i}^{N} p(D_i) D_i^3 \Delta D_i \tag{3.1}$$

$$\rho_L \frac{u_{inj}^3}{2} A_{inj} = \frac{\pi}{12} n \rho_L u_L^3 A \sum_i^N p(D_i) D_i^3 \Delta D_i$$
$$+ n u_L A \pi \sigma \sum_i^N p(D_i) D_i^2 \Delta D_i + K' \mu_L \left\langle \left(\frac{\partial u}{\partial y} \right)^2 \right\rangle (SprayVolume) \quad (3.2)$$

The conservation of mass equation (3.1) equates the inlet mass flow rate to the integral of the mass flow rate of all droplets, which follow a probability distribution, $p(D_i)$. The conservation of energy equation (3.2) similarly equates the inlet kinetic energy to the summation of the droplet kinetic energy, surface tension energy, and the energy advected by viscous dissipation (Lee and Robinson (2010)).

While the swirling flow control volume will look significantly different, the conservation equations will not change, as swirling jet atomization only relies on the liquid properties and velocities, akin to the straight flows.

By solving for number flow rate, n, from the conservation of mass equation (3.1) and substituting into the conservation of energy equation (3.2), the following quadratic formula is found:

$$D_{32} = \frac{3\sigma + \sqrt{9\sigma^2 + K' \rho_L \mu_L u_L^2 \frac{u_{inj}^2 - u_L^2}{2}}}{\rho_L \frac{u_{inj}^2 - u_L^2}{2}} \quad (3.3)$$

The quadratic formula for straight and swirling atomizing flows (Equation 3.3) computes Sauter mean diameter in meters, given a local velocity, liquid injection conditions, and liquid material properties (Lee and Robinson (2010)). Here, σ is the surface tension between the atomizing liquid and ambient gas, ρ_L is the liquid density, μ_L is the liquid viscosity, K' is the viscous dissipation tuning parameter, u_L is local liquid velocity, and u_{inj} is the liquid injection velocity.

Chapter 4

METHODS

4.1 Volume-of-Fluid Liquid Core Computation

In this work, the volume-of-fluid model in ANSYS Fluent is used to resolve the intact liquid core of all atomization geometries. This method computes the liquid trajectory in the continuous, or Eulerian, frame where the velocity field is coupled with the pressure field. It is assumed that both the gas and liquid phases are immiscible fluids. Thus, one set of momentum equations and a scalar transport equation for the volume fraction of each phase is sufficient to resolve the liquid trajectory as well as the liquid-gas interface (Fluent (2011)).

To track the trajectory of the liquid phase and the liquid-gas interface, a transport equation from the liquid volume fraction is computed.

$$\frac{\partial \alpha_L}{\partial t} + \overrightarrow{v} \cdot \nabla \alpha_L = \frac{S_{\alpha_L}}{\rho_L} \tag{4.1}$$

The volume fraction transport equation (4.1) equates the advection of the liquid volume fraction due to the velocity field to source term on the right hand side. In the case of liquid injection, the source term is the injector inlet mass flow rate. This equation is used to compute the volume fraction of liquid in each computational cell.

The gas volume fraction is not solved with a transport equation, but follows a simple constraint to maintain conservation of mass.

$$\alpha_g + \alpha_L = 1 \tag{4.2}$$

Equation (4.2) is used to compute the volume fraction of gas in each cell, which depends directly on the transport equation for the liquid phase volume fraction.

A single momentum equation is shared by both the liquid and gas phases where the density of the mixture in each cell is dictated by the liquid volume fraction.

$$\rho = \alpha_L \rho_L + (1 - \alpha_L)\rho_g \tag{4.3}$$

Similarly, the mixture viscosity is dictated by the liquid phase volume fraction.

$$\mu = \alpha_L \mu_L + (1 - \alpha_l)\mu_g \tag{4.4}$$

The volume fraction averaged density (Equation 4.3) and viscosity (Equation 4.4) in each cell is used in the momentum equation to compute the velocity field.

$$\frac{\partial}{\partial t}(\rho \overrightarrow{v}) + \nabla \cdot (\rho \overrightarrow{v}\,\overrightarrow{v}) = -\nabla \cdot p + \nabla \cdot \left[\mu\big(\nabla \overrightarrow{v} + \nabla \overrightarrow{v}^T\big)\right] + \rho \overrightarrow{g} + \overrightarrow{F} \tag{4.5}$$

The momentum equation (4.5) equates the advection of the mixture momentum $\left(\frac{\partial}{\partial t}(\rho \overrightarrow{v}) + \nabla \cdot (\rho \overrightarrow{v}\,\overrightarrow{v})\right)$ to the pressure field gradient effects $\big(-\nabla \cdot p\big)$, the diffusion of the mixture momentum $\left(\nabla \cdot \left[\mu\big(\nabla \overrightarrow{v} + \nabla \overrightarrow{v}^T\big)\right]\right)$, and the body forces exerted on the mixture $\big(\rho \overrightarrow{g} + \overrightarrow{F}\big)$. For all volume-of-fluid computations in this work, the body force terms are neglected.

In addition to the momentum equation (4.5), scalar transport equations of turbulence properties are solved to model the turbulence inherent to atomizing flows. The turbulence variables are shared both the liquid and gas phases

An implicit interpolation method is used to compute the face flux of liquid volume fraction at each cell. The implicit method requires the liquid phase volume fraction at each iteration and thus can be computed iteratively as a scalar transport equation.

$$\frac{\alpha_L^{n+1} - \alpha_L^n}{\Delta t} V + \sum_f (U_f^{n+1} \alpha_{L,f}^{n+1}) = 0 \tag{4.6}$$

In Equation (4.6), the time-rate of change difference between the liquid volume fraction in an adjacent cell and the cell in question multiplied by the cell volume $(\frac{\alpha_L^{n+1}-\alpha_L^n}{\Delta t}V)$ and the sum of the volume fraction flux through the cell faces shared by both cells $\left(\sum_f (U_f^{n+1}\alpha_{L,f}^{n+1})\right)$ must equate to zero to conserve mass as well as compute the distribution of the liquid volume fraction.

4.2 Determination of Atomization Locations

For diesel and water straight flows the atomization criterion is defined as where the maximum gradient of the velocity field causes local shear forces to exceed the surface tension force on the all-liquid core. This leads to atomization on the periphery and tip of the spray. The tip length of the spray is defined as where the minimum axial derivative of the axial velocity at the center of the spray occurs. The radial atomization for straight sprays occurs in the shear layer, which surrounds the minimum radial derivative of the axial velocity profiles.

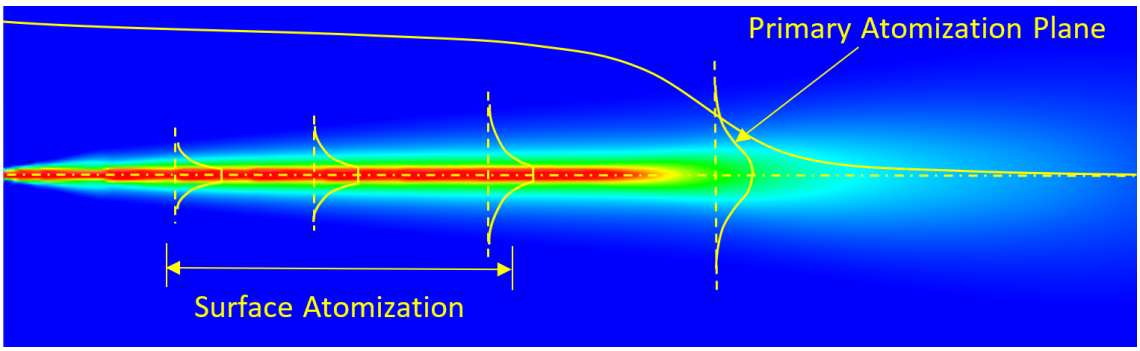

Figure 4.1: A schematic of the computational protocol to be applied to straight jets. First, the continuous liquid part is computed, then local D32 (from Equation (3.3)) and liquid velocity are used to initiate the discrete phase simulation at the surface and at the primary atomization plane.

Figure 4.1 displays a schematic of the computational protocol to be applied to straight jets. The current model utilizes fifty-percent of the minimum radial derivative value as the bounds of the shear layer.

This constraint was determined by comparing the computed velocity profiles and derivatives to experimental droplet distributions, as well as implementation into the final spray modeling, which is validated with experimental results for the respective spray conditions.

The atomization criterion for swirling flows is also defined by the maximum derivatives of the velocity fields. However, since hollow-cone swirling sprays are highly unstable, it can be appropriate to define an initial break-up area, followed by additional area injections to capture the atomization of additional ligaments that will shear from the liquid sheet along with droplets.

In swirling flows, atomization occurs very close to the injector followed closely by secondary atomization. Thus, the downstream injection areas in the Lagrangian solver are needed, as displayed approximately in Figure 4.2. The width of each injection area is taken between the maximum and minimum derivatives of the flow field. Since the spray will have momentum in the axial, radial, and tangential directions, a total derivative term is defined as the sum of the derivative of each velocity component in each direction.

$$\frac{d\overline{U}}{d\overline{X}} = \frac{du_1}{dx_1} + \frac{du_2}{dx_1} + \frac{du_3}{dx_1} + \frac{du_1}{dx_2} + \frac{du_2}{dx_2} + \frac{du_3}{dx_2} + \frac{du_1}{dx_3} + \frac{du_2}{dx_3} + \frac{du_3}{dx_3} \tag{4.7}$$

Equation (4.7) is computed and extracted from line surfaces perpendicular to the liquid sheet to find the bounds of the area injections. The bounds are defined as the locations where minimum and maximum values of $\frac{d\overline{U}}{d\overline{X}}$ are found on the perpendicular line surfaces.

Each atomization area and annulus, determined by the proper atomization criterion in both the straight and swirling sprays, are separated into equidistant points. The velocity information at these points are used to compute the local drop size using Equation (3.3), mass flow rate (Equation 4.8), and number flow rate (Equation 4.9).

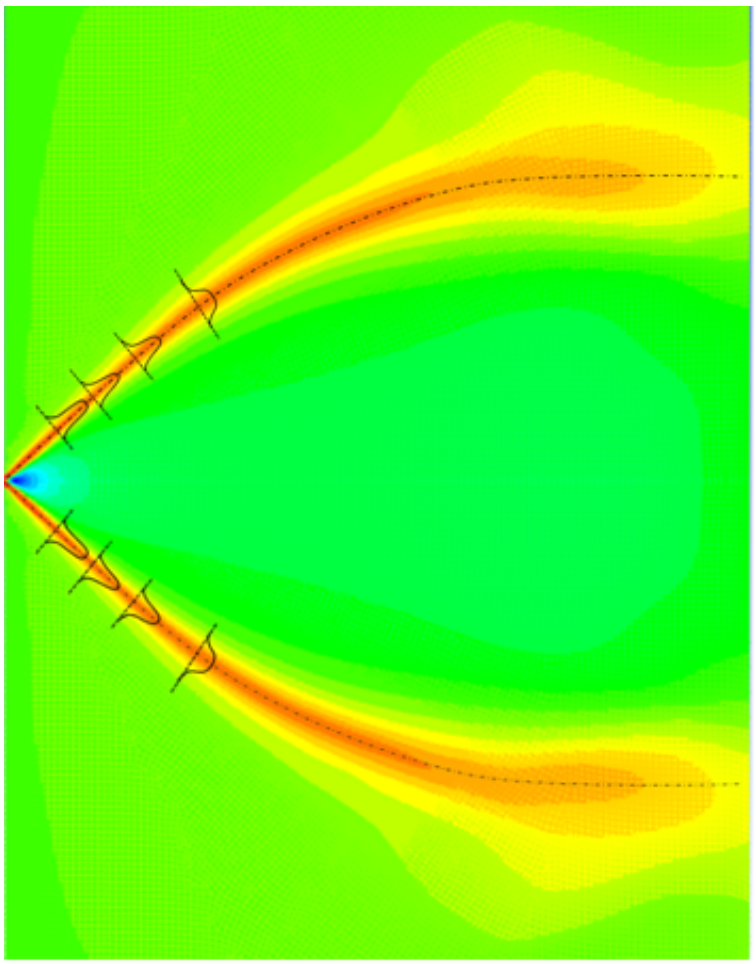

Figure 4.2: A schematic of the computational protocol to be applied to swirling sprays. Velocity profiles are used along the liquid sheet, to initiate the discrete phase computations, as schematically shown (locations are approximate, for illustration purposes).

Then, point injections are created at these coordinates and tracked as Lagrangian point particles.

4.3 Discrete Phase Injection Set-up

The sum of the mass flow rate of each injection in the primary spray modeling using the Discrete Phase Model (DPM) in ANSYS Fluent must equal the mass flow rate at the inlet of the injector.

The mass flow rate of each injection in the DPM computation is calculated as a function of the respective injection velocity magnitude.

$$\dot{m}_i = \dot{m}_{inlet} \frac{\overline{u}_i}{\sum_{i=1}^{N} \overline{u}_i} \tag{4.8}$$

Equation (4.8) computes the mass flow rate of each injection into the domain, ensuring that the sum of each injection mass flow rate is equal to the injector inlet mass flow rate. This also ensures that the mass flow rate of the discrete phase simulation is the same as the experimental mass flow rate. The subscript, i, indicates the local mass flow rate and velocity magnitude at each respective atomization location.

The local drop size to be injected is computed using the local velocities at the discretized atomization locations, defined by the points of atomization outlined in Section 4.2. For straight and swirling flows, the quadratic formula (Equation 3.3) is utilized.

Additionally, a number flow rate is used to define the number of drops introduced into the domain per second.

$$n = \frac{\dot{m}_i}{\frac{\pi}{6} \rho D_{32,i}^3} \tag{4.9}$$

The number flow rate (Equation 4.9) is necessary to determine the unsteady particle tracking time step to use in order to ensure a realistic droplet number density. The unsteady particle tracking time step is defined as the largest time step in which all point injections will introduce at least one full particle into the domain per time step (i.e. $n = 2.5x10^5$ particles per second; thus, $\Delta t_{particle} = 1x10^{-5}$ seconds).

4.4 Discrete Phase Model

The Discrete Phase Model (DPM) in ANSYS Fluent is used to track the trajectory of the spherical particles defined by the volume-of-fluid atomization locations, respective velocity information, and computed drop size by the appropriate quadratic formula. This model tracks the fluid particles in a Lagrangian reference frame as a secondary phase in the primary, continuous (Eulerian) gas phase (Fluent (2011)).

The particle trajectory is computed using a particle force balance transport equation in a Lagrangian frame of reference.

$$\frac{du_p}{dt} = F_D(u - u_p) + F_x \tag{4.10}$$

Equation (4.10) is simplified here as all computations in this work exclude forces due to gravity. The particle velocity gradient depends on the drag force exerted upon the particle by the gas phase and additional force terms that may be incorporated in the computation.

$$F_D = \frac{18\mu}{\rho_p d_p^2} \frac{C_D Re}{24} \tag{4.11}$$

The drag force, computed using Equation (4.11), relies on the particle Reynolds number and drag coefficient, C_D. The drag coefficient empirical formula assumes that all particles remain spherical throughout the domain.

$$Re = \frac{\rho d_p \mid u_p - u \mid}{\mu} \tag{4.12}$$

$$C_{D,sphere} = \begin{cases} 0.424 & Re < 1000 \\ \frac{24}{Re}(1 + \frac{1}{6}Re^{2/3}) & Re \geq 1000 \end{cases} \tag{4.13}$$

Equation (4.12) computes the particle Reynolds number as a function of the gas viscosity, the liquid density, and the relative velocity between the particle and continuous gas. Equation (4.13) computes the particle drag coefficient as a function of the particle Reynolds number.

The additional force terms that can be incorporated into Equation (4.10) are the virtual mass and Saffman lift forces. A pressure gradient force could also be included, but is only appropriate when the density of the continuous phase is larger than the density of the discrete phase. The virtual mass force is the force that is required to accelerate the gas surrounding a particle.

$$F_x = \frac{1}{2}\frac{\rho}{\rho_p}\frac{d}{dt}(u - u_p) \tag{4.14}$$

As seen in Equation (4.14), the virtual mass force required to accelerate the gas surrounding the liquid particles is a function of the gas to liquid density ratio and the time derivative of the local velocity differences.

$$\overrightarrow{F}_x = \frac{2K\nu^{1/2}\rho d_{ij}}{\rho_p d_p (d_{lk}d_{kl})^{1/4}}(\overrightarrow{v} - \overrightarrow{v}_p) \tag{4.15}$$

The Saffman lift force (Equation (4.15)) characterizes the lift forces due to shear between the particle and the continuous phase. Here, $K = 2.594$ and d_{ij} is a local deformation tensor in the continuum.

The discrete random walk (DRW) model is enabled to model the dispersion of the particles due to to turbulent fluctuations in the continuous phase. When enabled, the trajectory equations of each particle is integrated using both the local mean and fluctuating components of the continuous velocity field at each iteration.

4.5 Diameter Statistics Calculations

To extract steady SMD distributions from the Discrete Phase Model simulations, a User Defined Memory (UDM) code is employed to track the number and drop size of each particle passing through each cell in the computational domain. The UDM is compiled into a library and hooked to the simulation to store the particle statistics. The code directly computes the SMD at each mesh point using the stored arrays of particle size and respective particle count.

$$SMD = \frac{\sum_{i=1}^{N} n_i d_i^3}{\sum_{i=1}^{N} n_i d_i^2} \tag{4.16}$$

The UDM code uses Equation (4.16) to compute the SMD at each mesh point. The full code can be found in Appendix C.

Chapter 5

WATER JET ATOMIZATION

5.1 Validation Data

The water jet atomization simulation is validated through the experimental results found by Ruff *et al.* (1991) for a water jet into air. The injector investigated is a round, straight jet with an inlet diameter of 9.5 mm with a nominal inlet velocity of 56.7 m/s. The experimental group used a double-pulsed holography measurement technique to determine drop size and velocity as a function of radial distance from the centerline at multiple planes of interest.

5.2 Volume-of-Fluid

A uniform Cartesian axisymmetric mesh with a cell area of 2.5×10^{-3} $[m^2]$ in the Volume-of-Fluid model is utilized in the liquid column calculation. The mesh is 2.5 meters long and 0.5 meters tall. Water at 56.7 m/s is sent into the quiescent, air-filled domain from an inlet with a diameter of 9.5 mm (Ruff *et al.* (1991)). The inlet turbulence intensity is set to 7.5 percent and uses the hydraulic diameter of the injector (9.5mm) to accurately model the turbulent viscosity ratio at the inlet. The realizable k-epsilon viscous model is used to model turbulence as the injector inlet has a Reynolds number of 54×10^4, thus the flow is fully turbulent. The implicit dispersed interface modeling is enabled to capture the liquid-gas interface. The field is solved in a steady state solver until convergence. A Coupled method with second order discretization solution scheme solves the flow, which couples velocity and pressure to determine the velocity distribution.

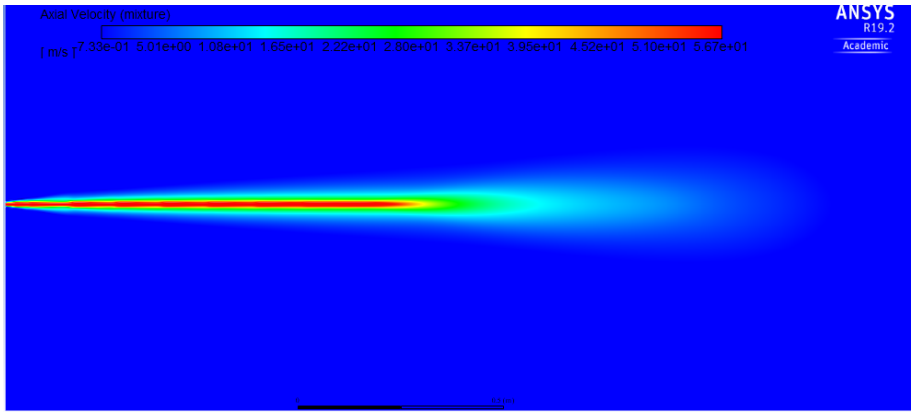

Figure 5.1: Contour of the axial velocity field computed using the VOF model in ANSYS Fluent for the water jet atomization with operating conditions matching experimental conditions (Ruff *et al.* (1991)).

Figure 5.1 displays the resulting axial velocity contour from the VOF computation using the operating conditions tested by Ruff *et al.* (1991) for water jet atomization. The data computed in this volume-of-fluid simulation is used to determine the atomization sites and velocities to be used in the discrete phase model.

5.3 Atomization Locations

The information computed in the VOF simulation is used to set up DPM injections to model the primary atomization process and Sauter mean diameter radial distributions in the near-injector region, which are compared to Ruff *et al.* (1991) distributions. The radial span of the surface atomization injection sites is contained within the shear layer of the liquid jet, which also captures the liquid-gas interface. A tested 50 percent of the radial derivative of the axial velocity ($\frac{du}{dy}$) has been selected to capture this shearing region, where it is hypothesized that atomization occurs. Figure 5.2 shows the radial velocity profile and the corresponding axial derivative taken at 5 diameters downstream to illustrate how the bounds of each injection annulus are determined. The radial locations associated to 50 percent of the minimum derivative in the radial direction are selected as the bounds for the surface atomization injections.

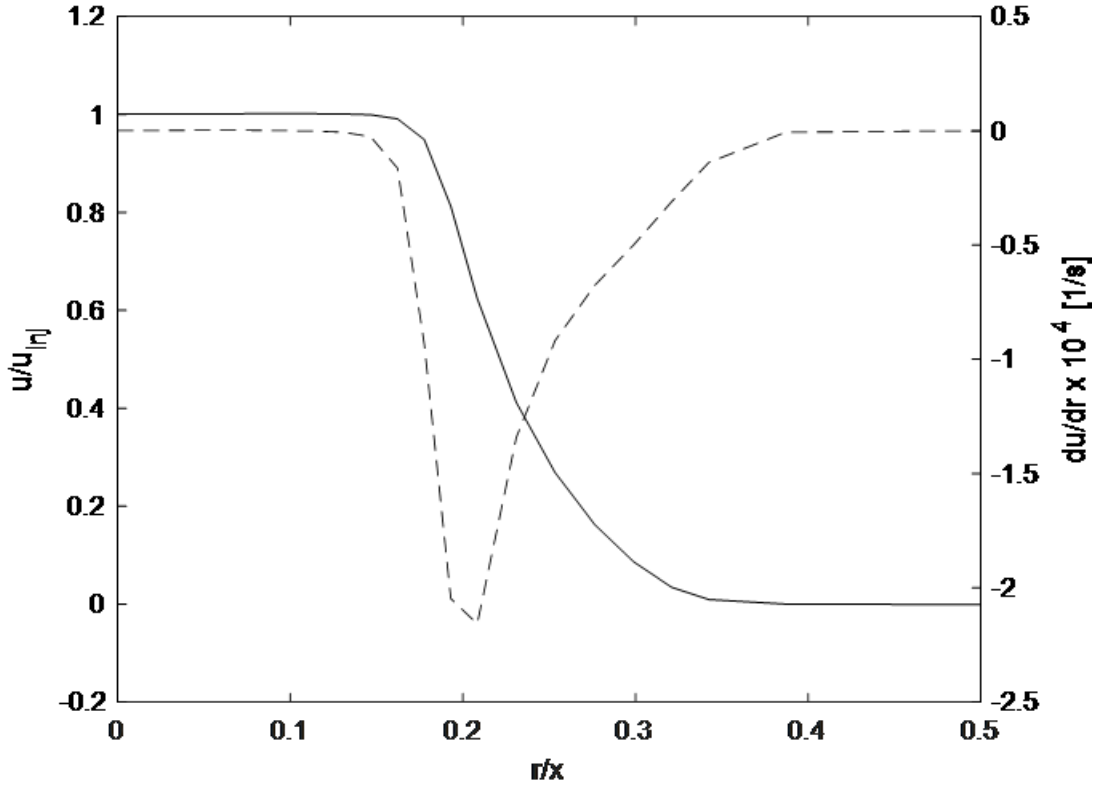

Figure 5.2: Computed normalized axial velocity (solid line) and radial derivative of the axial velocity (dashed line) as a function of normalized radial distance taken at 5 diameters downstream of the injector.

The break-up injection site axial location is dictated by the minimum axial derivative of the axial velocity ($\frac{du}{dx}$), depicted in Figure 5.3. Similarly, the width of the primary injection area is dictated by 50 percent of the radial derivative of the axial velocity. The axial locations of the surface atomization are selected based on the break-up length such that there are five surface atomization sites evenly distributed between the inlet and the break-up length. The axial locations of the surface injections are five, ten, twenty, forty, and eighty diameters downstream while the break-up distance is 104 diameters downstream. All six velocity profiles can be found in Appendix D.

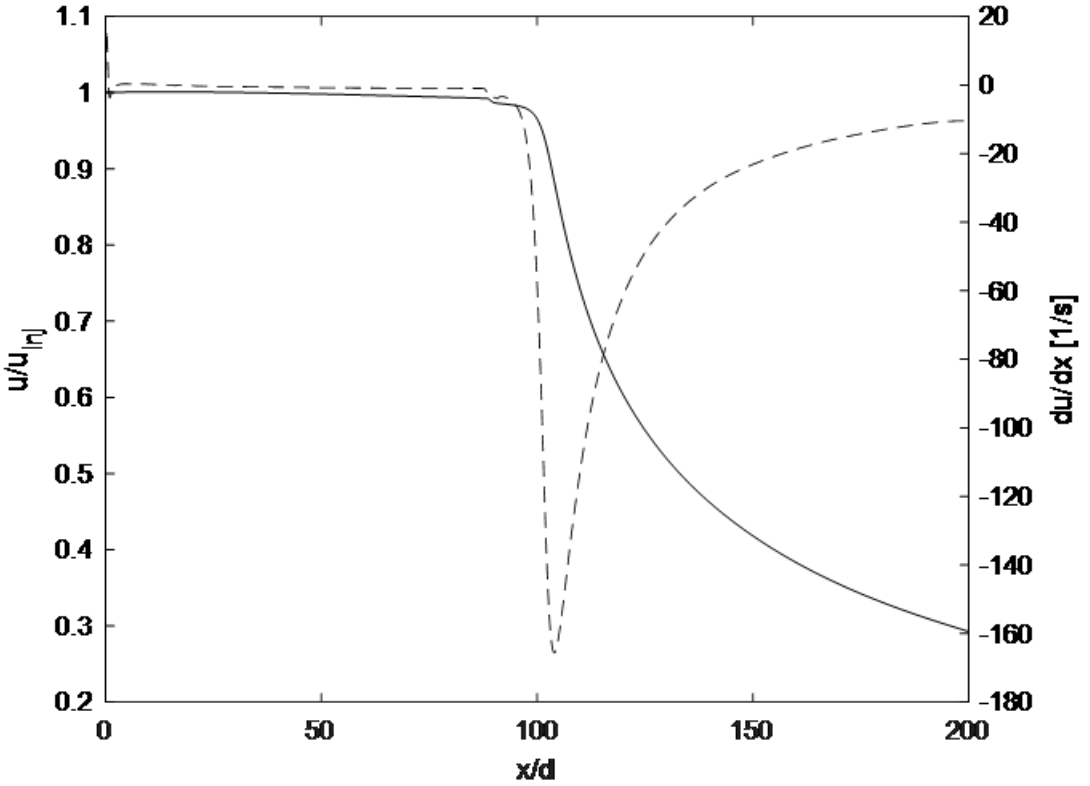

Figure 5.3: The computed normalized axial velocity (solid line) and the axial derivative of the axial velocity (dashed line) as a function of normalized distance along the center line.

5.4 Discrete Phase Model

The surface atomization annuli and break-up injection area are split evenly into five surface atomization injection sites. The local velocity components at each point are used to compute the SMD of the injection using Equation (3.3). The viscous dissipation constant, K', in the quadratic formula used is K'=0.1. The properties of water at standard atmospheric conditions are utilized in the quadratic formula and are as follows: Density- $\rho = 998 \quad kg/m^3$, Viscosity- $\mu = 0.001 \quad Pa \cdot s$, and Surface tension- $\sigma = 0.076 \quad N/m$ (EngineeringToolBox (2003)).

$$\dot{m}_{bp} = \rho_L A_{bp} \overline{u}_{bp} \tag{5.1}$$

The mass flow rate to be injected from the tip of the liquid column, $\dot{m}_{bp}$, is computed using the injection area, A_{bp}, water density, ρ_L, and average velocity of the injection area, $\overline{u}_{bp}$, as shown in Equation (5.1).

$$\dot{m}_{bp,i} = \dot{m}_{bp} \frac{u(y)_i}{\sum_{i=1}^{5} u(y)_i} \tag{5.2}$$

The total mass flow rate of the break-up injection is split amongst the point injections at the discretized radial coordinates as a ratio of the point velocity to the sum of all five point's velocities (Equation (5.2)).

$$\dot{m}_{surface,i} = (\dot{m}_{inj} - \dot{m}_{bp}) \frac{u(x)_{cl,i}}{\sum_{i=1}^{5} u(x)_{cl,i}} \tag{5.3}$$

Similarly, the total mass flow rate of the surface injection annuli is computed as a ratio of the center line velocity at the axial location of the surface injections to the sum of all five center line velocities multiplied by the remaining available mass flow rate (Equation (5.3)).

$$\dot{m}_{surface,i,j} = \dot{m}_{surface,i} \frac{u(y)_{i,j}}{\sum_{j=1}^{5} u(y)_{i,j}} \tag{5.4}$$

The mass flow rate of each point injection along each surface atomization injection annuli is then split in the same fashion as the point injection mass flow rates at the break-up location using Equation (5.4).

$$n = \frac{\dot{m}}{\frac{\pi}{6} \rho_L D_{32}^3} \tag{5.5}$$

Additionally, the number flow rate, n, for each point injection is computed to determine the unsteady particle time step (Equation (5.5)), where $\dot{m}$ and D_{32} correspond to the mass flow rate and computed SMD for the point injection in question. Each injection should introduce at least one full particle into the domain per time step. From the computed number flow rate for each point injection, an unsteady particle time step of $10ms$ is selected.

The mass flow rate, coordinates, velocity components, drop size, and number flow rate for each point injection at the respective axial location for the surface and break-up atomization locations are tabulated in Appendix E. In the discrete phase model, the axial and radial velocities, the axial location, the radial location, the SMD, and mass flow rate are used as inputs for all point injections. The realizable $k - \epsilon$ turbulence model is used to model the turbulence in the domain. Second-order discretization is used to solve the trajectory of the Lagrangian Point Particles. Unsteady particle tracking in a steady-state solver is used with a particle time step of 10 milliseconds. Additionally, discrete random walk and the Saffman lift force models are applied to each injection to allow for realistic dispersion of the particles.

5.5 Results and Discussions

The discrete phase simulation is run until convergence, marked by when the data displayed by the user-defined memory Sauter mean diameter radial distributions at the experimental interrogation planes become constant and no longer change.

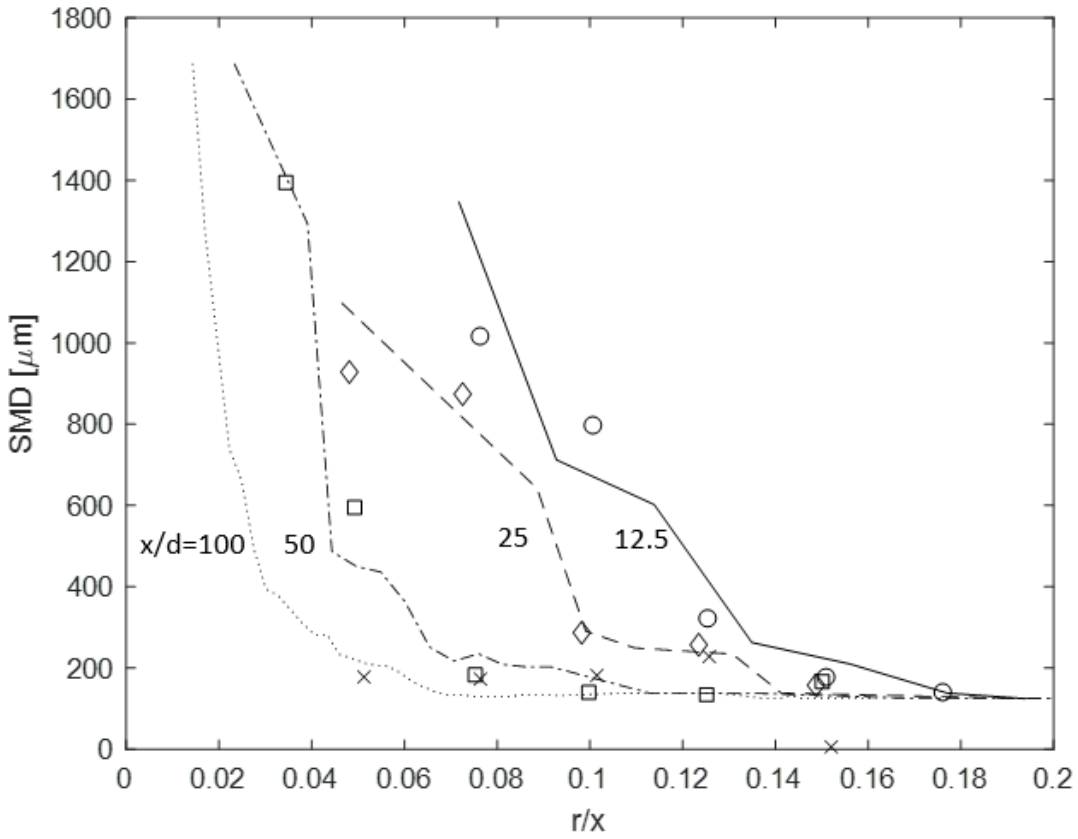

Figure 5.4: The computed SMD radial distributions compared to experimental results. The lines represent the calculated result and the data symbols represent the experimental data (Ruff *et al.* (1991)).

From the data, it be can seen that the drop velocities and also SMD are high near the liquid column surface then both decrease in the radial direction.

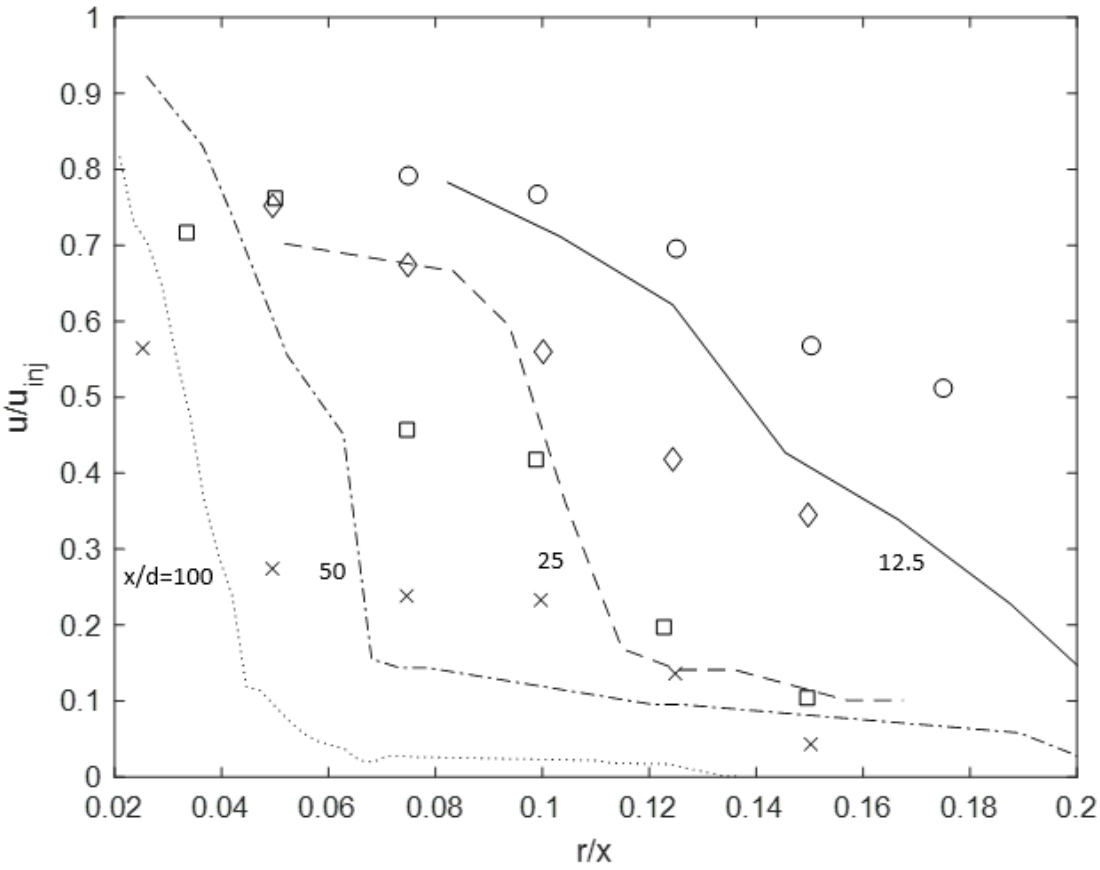

Figure 5.5: The computed particle velocity radial distributions compared to experimental results. The lines represent the calculated result and the data symbols represent the experimental data (Ruff *et al.* (1991)).

Equation (3.3) shows that large liquid velocities close to the surface will produce or be associated with large droplets, and computations reflect this observation, since in the continuous liquid jet simulation the centerline velocity is highest and then decreases toward the periphery. Conversely, low liquid velocities are correlated with small SMD, again as shown in Figure 5.4. The droplet velocities are tracked in the Lagrangian part of the simulation, and reflects the drop velocity (and trajectory) with

the initial liquid velocity retarded by the drag with the surrounding gas (air).

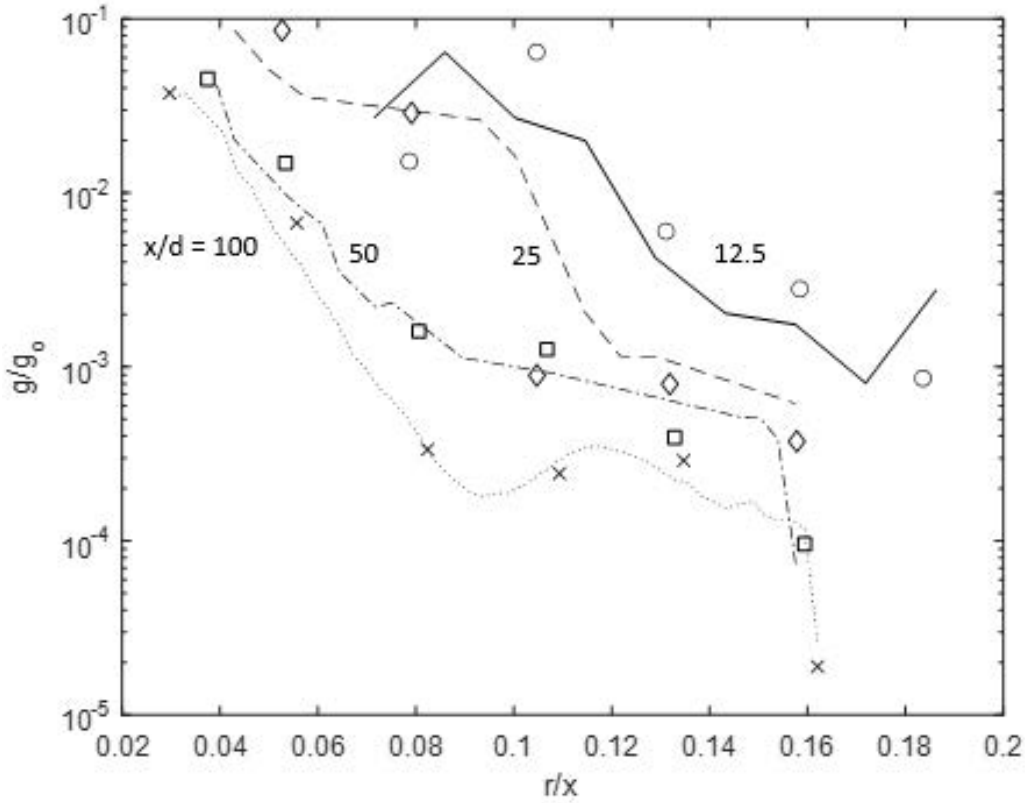

Figure 5.6: The computed particle flux radial distributions compared to experimental results. The lines represent the calculated result and the data symbols represent the experimental data (Ruff *et al.* (1991)).

It can be again seen in Figure 5.4 that this the droplet behavior is fairly well simulated in the current method, keeping in mind that for both the drop size and velocity there are some perturbations relative to the average due to various factors. For example, the drop velocity is underestimated in Figure 5.5. Computationally, the turbulent fluctuations can introduce variations in the drop size and velocity. This can easily be taken into account (Lee and An (2016)), but has not been added in the current computational module. Also, the measurement by Ruff *et al.* (1991) was made using double-pulsed holography so that sampling and data analyses inherently contain some amount of errors as well. In Figure 5.6, the computed normalized droplet flux versus radial position at the measurement planes.

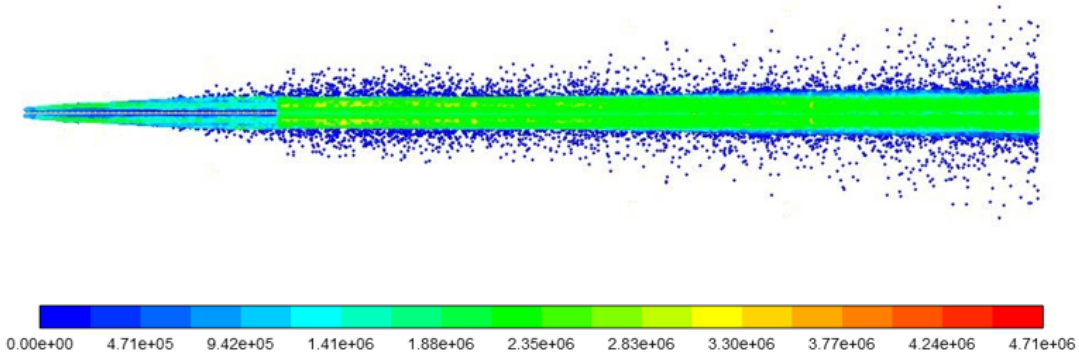

Figure 5.7: Contour plot of the drop number density for the straight water jet atomization simulation. Note that the inner part of the spray has nearly constant drop number density beyond roughly 100 diameters downstream, indicating the end of the liquid core, both physically and computationally.

It can be seen that there is good agreement between the measured and computed droplet flux, despite an underestimate in the droplet velocities. This is likely a result of the particle velocity having less effect on the flux values compared to the droplet size, illustrated in Equation 5.6 where u_p is the droplet velocity, d_p is the droplet diameter, and A_p is the droplet cross-sectional area.

$$g = \frac{u_p d_p}{A_p} \tag{5.6}$$

In spite of these factors, the agreement between the simulation and data is encouraging where the SMD are in quite good agreement with very low computational cost and grid requirements. Then, Equation (3.3) is a validated expression of the drop size, based on fundamental conservation principles, so that the current agreement and level of accuracy for the drop size are expected.

The spray shape can also be visualized in the current simulation, by contour-plotting for example the drop number density as shown in Figure 5.7.

The transition from continuous liquid core to dispersed droplets is abrupt at roughly 100 diameters downstream, and the reason for this is the atomization criterion corresponding to the maximum negative centerline velocity gradient has been applied at this point. It can also be observed that the droplet number density following this atomization criterion of liquid core break-up is an order of magnitude higher than surface-atomized droplets in the periphery of the liquid jet.

Chapter 6

DIESEL ATOMIZATION

6.1 Validation Data

Two data sets are used to validate the diesel atomization protocol. The data set from Martinez *et al.* (2017) is used to validate the radial distribution of SMD in the near injector region. This investigation is of a diesel injector with a inlet diameter of 0.186 mm with a nominal injection velocity of roughly 270 m/s into ambient air at standard temperature and pressure. The diesel injection velocity was computed using the pressure drop across the injector (49.9 MPa), diesel fuel density (820 kg/m^3), and an assumed discharge coefficient of 0.8, using Equation (6.1).

$$u_{inj} = C_d\sqrt{\frac{2\Delta p}{\rho_L}} \tag{6.1}$$

The data set from Lee and Park (2002) is used to validate the axial distribution of SMD of a atomizing diesel jet. This investigation is of a diesel injector with a inlet diameter of 300 μm with a nominal injection velocity of 266.24 m/s into ambient air at standard temperature and pressure.

6.2 Volume-of-Fluid

As the average end behavior of all straight jets are marked by a penetration depth of 100-150 diameters downstream (Ruff *et al.* (1991)), it is a logical and time-saving decision to simply scale the water jet VOF fields by the ratio of the injector diameters and injection velocities.

To match the experimental conditions of Martinez *et al.* (2017), the width and length of the flow fields are scaled by the ratio of the diesel injector diameter (0.186 mm) to the water injector diameter (9.5 mm) from Ruff *et al.* (1991). Similarly, the velocity fields are scaled by the ratio of the diesel injection velocity (270 m/s) to the water injection velocity (56.7 m/s). From the scaled velocity field for Martinez *et al.* (2017), the field was scaled once again to match the experimental conditions investigated by Lee and Park (2002) by the ratio of the injector diameters and injection velocities. When considering the turbulence levels of the diesel injections ($Re_{inlet} = 1.6 \times 10^4$ and $Re_{inlet} = 2.5 \times 10^4$ for the Martinez *et al.* (2017) and Lee and Park (2002) comparison cases, respectively), the diesel injection cases are also fully turbulent, validating the scaling of the water jet VOF fields.

6.3 Atomization Locations

As described in Chapter 5, the data in the VOF simulations is used to determine the atomization locations of the jet by applying atomization criterion. The radial span of the surface atomization injection sites is contained within the shear layer of the liquid jet, which also captures the liquid-gas interface. Again, 50 percent of the radial derivative of the axial velocity ($\frac{du}{dy}$) has been selected to capture this shearing region, where it is hypothesized that atomization occurs. Figure 6.1 shows the radial velocity profile and the corresponding axial derivative taken at 5 mm downstream to be validated by Martinez *et al.* (2017) data to illustrate how the bounds of each injection annulus are determined. The radial locations associated to 50 percent of the minimum derivative in the radial direction are selected as the bounds for the surface atomization injections.

The break-up injection site axial location is dictated by the minimum axial derivative of the axial velocity ($\frac{du}{dx}$), depicted in Figure 6.2.

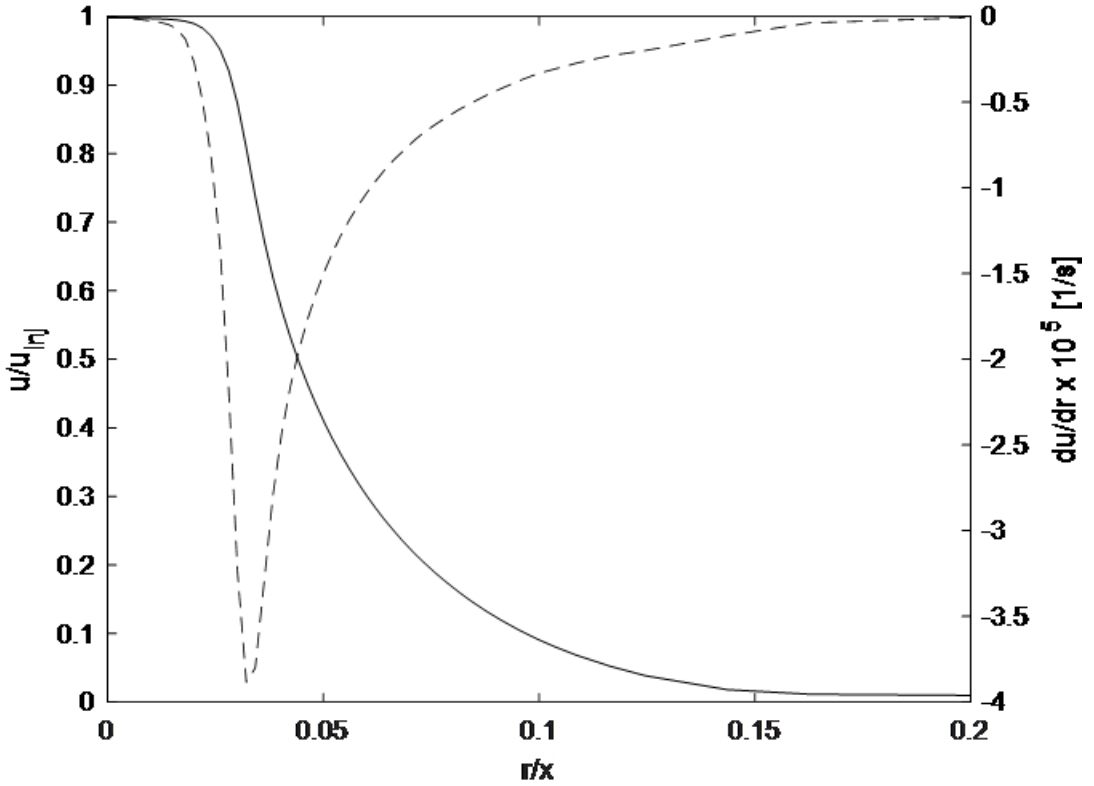

Figure 6.1: Computed normalized axial velocity (solid line) and radial derivative of the axial velocity (dashed line) as a function of normalized radial distance taken at 5 mm downstream of the injector for Martinez *et al.* (2017) simulation.

Similarly, the width of the primary injection area is dictated by 50 percent of the radial derivative of the axial velocity. The axial locations of the surface atomization are selected based on the break-up length such that there are three surface atomization sites evenly distributed between the inlet and the break-up length. The axial locations of the surface injections are 5 mm, 7.5 mm, and 15 mm downstream for Martinez *et al.* (2017) while the break-up distance is 21.6 mm downstream. All four velocity profiles can be found in Appendix F. Similarly, the axial location of the surface injections for Lee and Park (2002) comparison are 8 mm, 12 mm, and 24 mm downstream with the break-up distance as 34.8 mm.

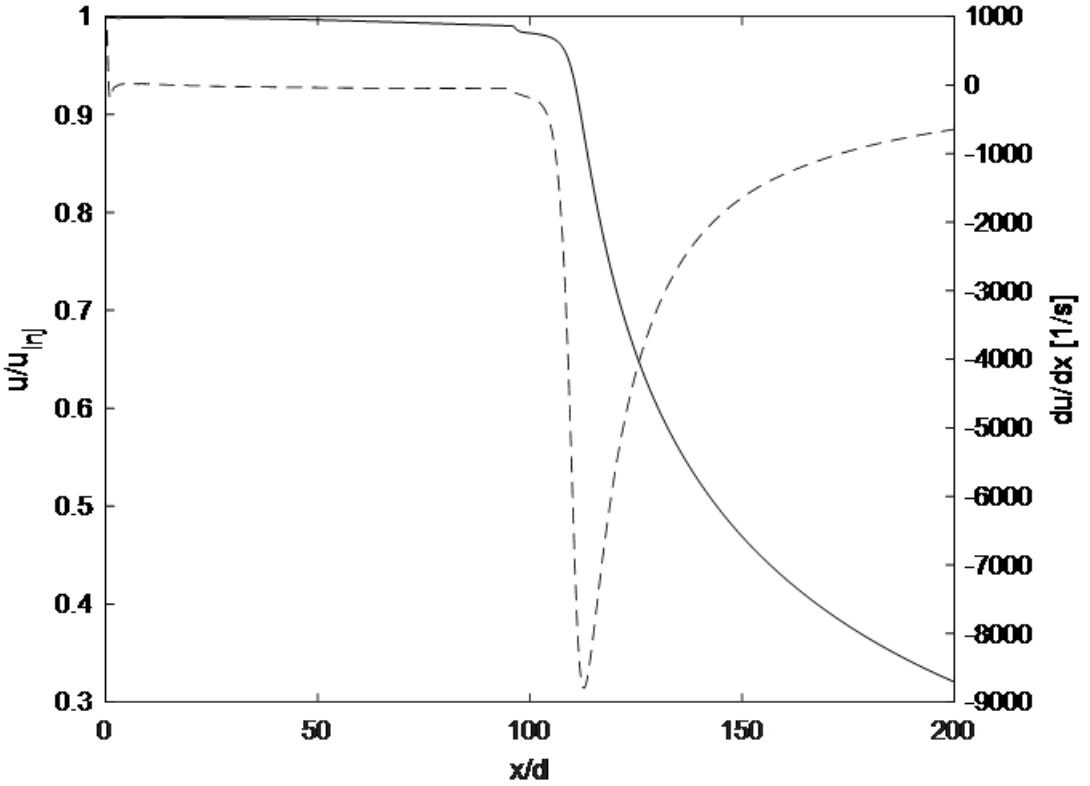

Figure 6.2: The computed normalized axial velocity (solid line) and the axial derivative of the axial velocity (dashed line) as a function of normalized distance along the center line for Martinez *et al.* (2017) simulation.

The velocity profiles for Lee and Park (2002) are not plotted as the tabulated information from the Martinez *et al.* (2017) case is simply scaled by the ratio of the inlet diameters and injection velocities.

6.4 Discrete Phase Model

The surface atomization annuli and break-up injection area are split evenly into seven atomization injection sites. The local velocity components at each point are used to compute the SMD of the injection using Equation (3.3). The viscous dissipation constant, K', in the quadratic formula used for the Martinez *et al.* (2017) validation case is 1.4×10^{-5}, while the dissipation constant used for the Lee and Park (2002) validation case is 5×10^{-5}. The fluid properties of diesel fluid were taken at 300 K for both test cases. Surface tension is $\sigma = 0.026 \quad N/m$ (Chhetri and Watts (2013)). Kinematic viscosity is $\mu = 0.0026 \quad Pa \cdot s$ (EngineeringToolBox (2003)). The fluid density is $\rho = 820 \quad kg/m^3$ (Martinez *et al.* (2017)).

The mass flow rate to be injected from the tip of the liquid column, $\dot{m}_{bp}$, is computed using the injection area, A_{bp}, diesel fuel density, ρ_L, and average velocity of the injection area, $\overline{u}_{bp}$, as shown in Equation (5.1). The total mass flow rate of the break-up injection is split amongst the point injections at the discretized radial coordinates as a ratio of the point velocity to the sum of all seven point's velocities (Equation (5.2)).

Similarly, the total mass flow rate of the surface injection annuli is computed as a ratio of the center line velocity at the axial location of the surface injections to the sum of all three center line velocities multiplied by the remaining available mass flow rate (Equation (5.3)). The mass flow rate of each point injection along each surface atomization injection annuli is then split in the same fashion as the point injection mass flow rates at the break-up location using Equation (5.4).

Additionally, the number flow rate, n, for each point injection is computed to determine the unsteady particle time step (Equation (5.5)), where $\dot{m}$ and D_{32} correspond to the mass flow rate and computed SMD for the point injection in question.

Each injection should introduce at least one full particle into the domain per time step. From the computed number flow rate for each point injection, an unsteady particle time step of 10^{-7} seconds is selected for both simulation cases.

The mass flow rate, coordinates, velocity components, drop size, and number flow rate for each point injection at the respective axial location for the surface and break-up atomization locations are tabulated in Appendix G for the Martinez *et al.*(2017) validation case. The information stored in the Martinez *et al.* (2017) injection tables are scaled to match the Lee and Park (2002) operating conditions and can found in Appendix H. In the discrete phase model, the axial and radial velocities, the axial location, the radial location, the SMD, and mass flow rate are used as inputs for all point injections. Unsteady particle tracking in a steady-state solver is used with a particle time step of 10^{-7} seconds is used in both simulations. The realizable $k - \epsilon$ turbulence model is used to model the turbulence in the domain. Second-order discretization is used to solve the trajectory of the Lagrangian Point Particles. Additionally, discrete random walk and the Saffman lift force models are applied to each injection to allow for realistic dispersion of the particles.

6.5 Results and Discussions

Both simulation cases are run until the computed SMD statistics using the user-defined memory code (Appendix C) become constant at the planes of interest. For the radial distribution case, the computed radial SMD distribution is compared to the experimental result from Martinez *et al.* (2017), where a reasonable agreement is found.

In Figure 6.3, it can be seen that the data near to the center line of the jet match experimental results with high accuracy.

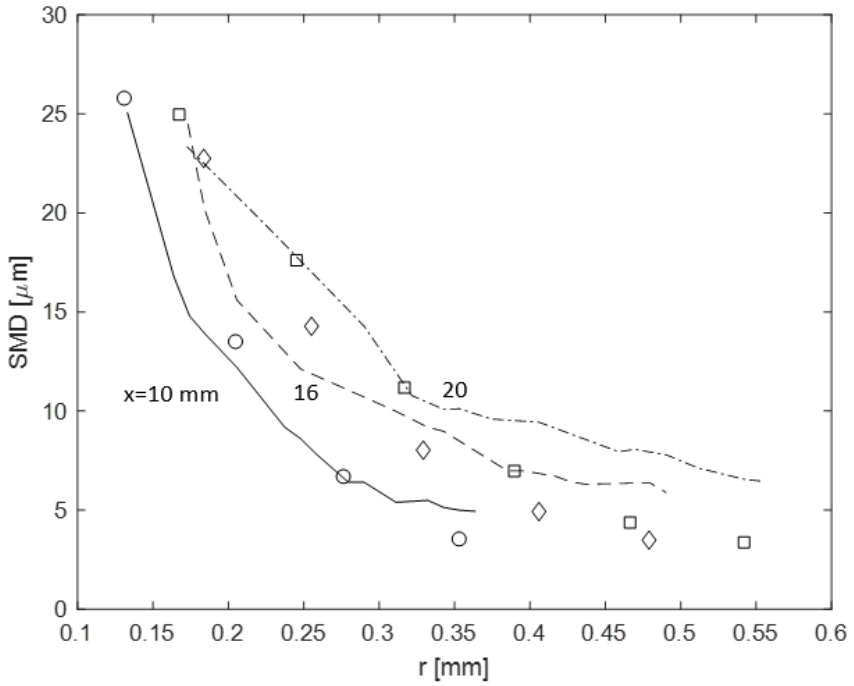

Figure 6.3: Computed SMD radial distribution compared to experimental results (Martinez et. al. 2017). The lines represent simulated results, where the solid line corresponds to 10 mm downstream, the dashed line corresponds to 16 mm downstream, and the dash-dotted line corresponds to 20 mm downstream. The data symbols represent experimental results, where the circles correspond to data taken at 10 mm downstream, the diamonds correspond to data taken at 16 mm downstream, and the squares correspond to data taken at 20 mm downstream (Martinez *et al.* (2017)).

However, the computed data further from the center line is over-estimated and can be explained through turbulent fluctuations in the experimental flow field that are not captured in the current computational method.

Similarly, the axial distribution case is compared to the axial SMD distribution data from Lee and Park (2002).

In Figure 6.4, it can be seen that the over-all trend of the computed axial SMD matches the experimental result with reasonable accuracy. Again, the computed D_{32} data is slightly under-estimated.

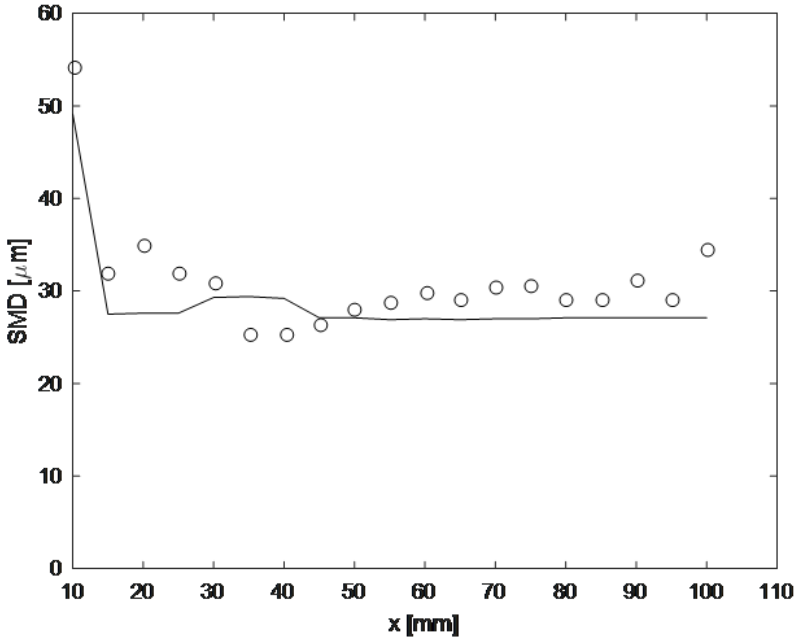

Figure 6.4: Computed axial SMD data (solid line) compared to experimental data (circles) from Lee and An (2016) .

This issue can be easily mitigated by slightly increasing the viscous dissipation constant, K', in the Quadratic Formula (Equation (3.3)).

The results obtained using the current computational protocol are encouraging for the estimation of diesel jet atomization droplet size distributions. Slight improvements can be made by accounting for the velocity turbulent fluctuations present in the shear layer when computing drop size using the Quadratic Formula.

Additionally, the droplet number density of the flow can be visualized using the current protocol.

Figure 6.5 displays the computed droplets colored by the number density value in the mesh cell in which they reside. The number density of each cell is computed using the same user-defined memory code used to computed the SMD.

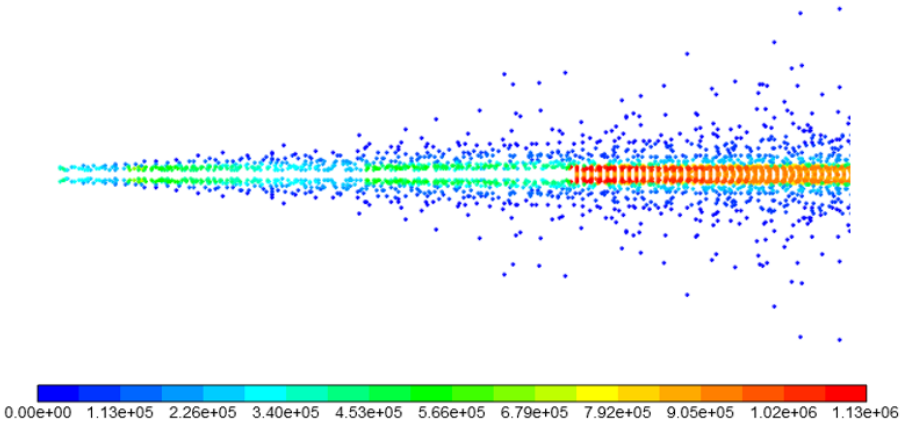

Figure 6.5: Computed drop number density contour. Note that the inner part of the spray has nearly constant drop number density beyond roughly 100 diameters downstream, indicating the end of the liquid core, both physically and computationally.

Similarly to the computed results for the water jet shown in Figure 5.7, there is a discontinuity in the number density past the break-up point, dictated by the maximum shear of the center line velocity in the axial direction. Again, the number density computed in the center of the spray slow is an order of magnitude higher than that of the droplets produced by surface atomization. This matches experimental trends where it has been found that a majority of droplets in a straight atomizing flow will originate from the tip of the liquid column at the break-up location.

Chapter 7

SWIRLING SPRAY ATOMIZATION

7.1 Validation Data

Experimental data from Marchione *et al.* (2007) is utilized to verify the swirling spray primary atomization model. Marchione *et al.* (2007) perform phase-Doppler particle anemometry on a kerosene, hollow-cone spray from a Delevan WDA $3.0 - 80°$ nozzle. The exit diameter is measured as 0.46 mm with the nominal flow rate of 10.2 L/h at 7 bars. The PDPA measures the droplet size and velocities of the hollow-cone spray.

7.2 Volume-of-Fluid

An axisymmetric mesh in the axisymmetric with swirl solution method in ANSYS Fluent is employed to compute the swirling liquid sheet trajectory. The computational grid is 40 mm by 40 mm with a region of fine mesh elements surrounding the expected liquid trajectory. This fine-mesh zone is used to ensure the liquid-gas interface is resolved with acceptable accuracy.

Figure 7.1 displays the computational grid for the swirling jet liquid sheet computation. Note the region of fine mesh elements, where the bounds are equally spaced about the expected liquid trajectory, dictated by the experimentally observed spray angle of 96° (Marchione *et al.* (2007)).

Implicit, dispersed interface modeling is used to emulate the dispersion of the secondary phase (kerosene) using the VOF method in ANSYS Fluent.

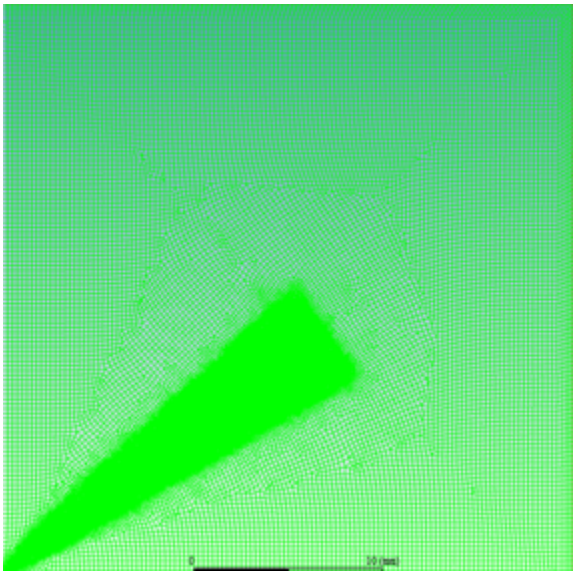

Figure 7.1: Computational axisymmetric grid to compute the liquid sheet trajectory using the volume-of-fluid method with swirl.

Due to the more complex turbulent behavior of a swirling jet, the k-omega viscous model was utilized, rather than the realizable k-epsilon model. The first order implicit transient solver with a small step size ($t = 10^{-6}$ seconds) was used to combat the intrinsic Kelvin-Helmholtz instability found in swirling jets in order to resolve the mean trajectory of the intact liquid sheet. The simulation is solved until the velocity fields are no longer visibly changing. The solution scheme utilized is the Coupled method with second order discretization, which couples velocity and pressure to determine the velocity distribution.

The inlet axial and swirl velocities are calculated from the given experimental flow rate, inlet diameter, and the spray cone angle, using Equations (7.1) and (7.2), respectively.

$$u = \frac{\dot{m}_{inj}}{\rho_L A_{inj}} \tag{7.1}$$

$$w = u \cdot tan\big(\theta/2\big) \tag{7.2}$$

In Equation (7.2), the swirl velocity depends on the experimentally observed spray cone angle, θ. The axial velocity was calculated as 17.05 m/s where the swirl velocity was found to be 18.9 m/s (considering the actual spray cone angle of $\theta = 96°$, as found experimentally by Marchione *et al.* (2007)) [ref]. The inlet is not assigned a radial velocity component as the centripetal forces produced by the swirling velocity component causes the liquid to travel in the radial direction. The inlet is assigned a 5 percent turbulence value and the hydraulic diameter of the injector (0.46 mm).

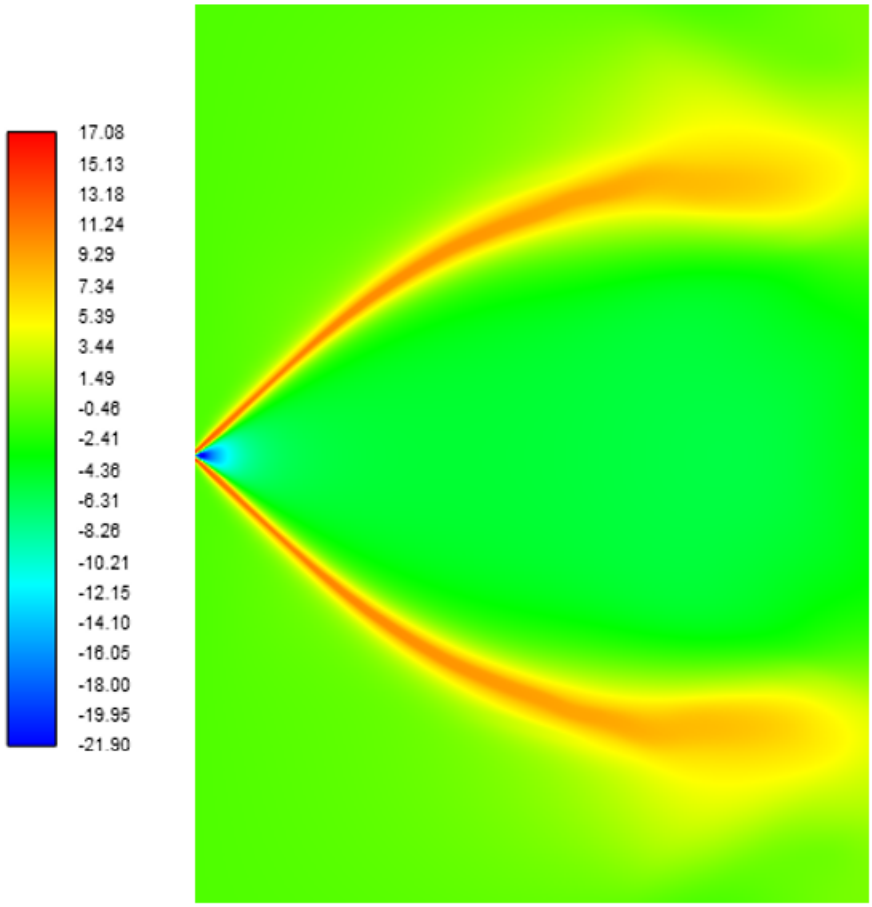

Figure 7.2: Computed axial velocity field contour from the volume-of-fluid computation in [m/s].

Figure 7.2 displays a contour of the resolved axial velocity field in [m/s] of the simplex atomizer liquid sheet computation. The volume-of-fluid velocity fields are used to determine the atomization locations, injection drop sizes, and injection velocities.

7.3 Atomization Locations

For swirl injection, the continuous liquid simulation includes the tangential velocity component at the injector exit, which produces the bell-shaped liquid "sheet", as shown in Figure 7.2. In swirl sprays, rapid atomization occurs due to this liquid sheet shape and multi-dimensional shear. For example, the drag coefficient in the liquid momentum balance tends to be large for swirl sprays, leading to rapid reduction in liquid velocity. This swirling motion and deceleration also cause atomization near the injector exit. Therefore, the atomization criterion for swirl sprays is the break-up starts again at the point of maximum negative velocity gradient ($x = 0.146$ mm), and continues to generate droplets along the liquid sheet. Therefore, 5 locations close to the injector, $x = 0.146$, 1, 2, 3, and 5 mm, are selected and the velocity profiles from the continuous liquid simulations at these locations are input into Equation 3.3. This will again furnish the initial drop size and velocities. The number flow rate for the droplets is prorated by the liquid centerline velocity at each injection points, so that the total number flow rate multiplied by the liquid density and droplet volume equals the injected mass flow rate.

Equation 4.7 is used to determine the periphery of the atomization areas, which are sampled at cross sections corresponding to the axial locations $x = 0.146$, 1, 2, 3, and 5 mm downstream, perpendicular to the liquid sheet.

The coordinates corresponding to the minimum and maximum derivative, computed by Equation 4.7, are the bounds of each injection area along the perpendicular cross sections, as seen in Figure 7.3.

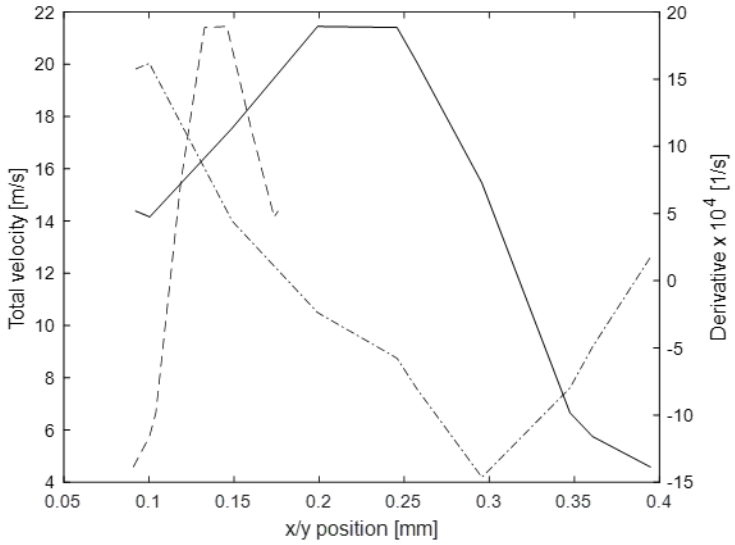

Figure 7.3: Computed velocity magnitude versus y-coordinate (solid line), velocity magnitude versus x-coordinate (dashed line), and total derivative versus y-coordinate (dot-dashed line) at x=0.146 mm downstream.

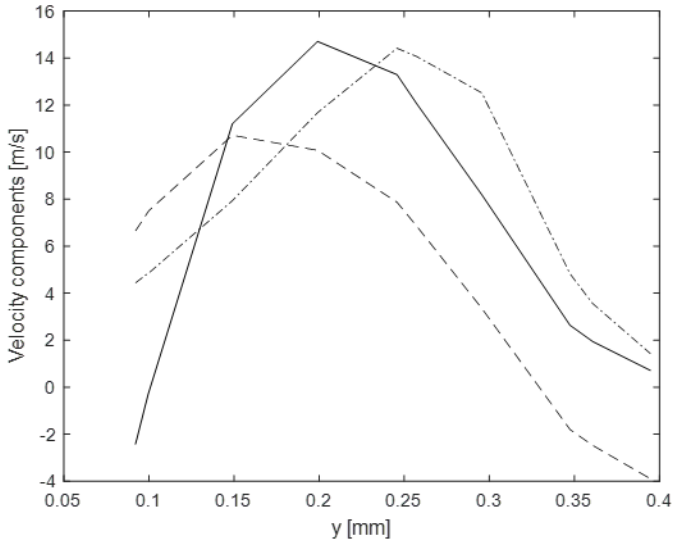

Figure 7.4: Computed axial velocity (solid line), radial velocity (dashed line), and tangential velocity (dot-dashed line) versus y-coordinate at x=0.146 mm downstream.

Each area is then split into six point injections and the velocity components at each point, displayed in Figure 7.4, are used to compute the point injection properties in the Discrete Phase Model. All five injection area velocity magnitude and velocity component figures can be found in Appendix I.

7.4 Discrete Phase Model

The five injection areas are split evenly into six atomization injection sites. The local velocity magnitude at each point is used to compute the SMD of the injection using Equation (3.3). The viscous dissipation constant, K', in the quadratic formula used is 1.65×10^{-3}. The fluid properties of kerosene fluid were taken at 300 K. Surface tension is $\sigma = 0.0275 \quad N/m$. Kinematic viscosity is $\mu = 0.00164 \quad Pa \cdot s$. The fluid density is $\rho = 820 \quad kg/m^3$ (EngineeringToolBox (2003)).

The mass flow rate to be injected from each injection area is computed as the ratio of the maximum velocity at the respective injection area to the sum of all maximum velocities in the injection areas times the injector mass flow rate using Equation (4.8). Similarly, the mass flow rate of each point injection is computed as the ratio of the respective point velocity magnitude to the sum of the six points velocity magnitudes in the same injection area multiplied by the mass flow rate of the injection area (Equation (7.3)).

$$\dot{m}_{point,i,j} = \dot{m}_i \frac{\overline{u}_{point,i,j}}{\sum_{j=1}^{6} \overline{u}_{point,i,j}} \tag{7.3}$$

Additionally, the number flow rate, n, for each point injection is computed to determine the unsteady particle time step (Equation (5.5)), where $\dot{m}$ and D_{32} correspond to the mass flow rate and computed SMD for the point injection in question. Each injection should introduce at least one full particle into the domain per time step. From the computed number flow rate for each point injection, an unsteady particle time step of 10^{-6} seconds is selected.

The mass flow rate, coordinates, velocity components, drop size, and number flow rate for each point injection are tabulated in Appendix J. In the discrete phase model, the axial, radial, and tangential velocities, the axial location, the radial location, the SMD, and mass flow rate are used as inputs for all point injections. Unsteady particle tracking in a steady-state solver is used with a particle time step of 10^{-6} seconds. The realizable $k-\epsilon$ turbulence model is used to model the turbulence in the domain. Second-order discretization is used to solve the trajectory of the Lagrangian Point Particles. Additionally, discrete random walk and the Saffman lift force models are applied to each injection to allow for realistic dispersion of the particles.

7.5 Results and Discussions

Again, the user-defined memory function (Appendix C) is employed to compute the simulated SMD distributions at the experimental measurement planes to compare to particle velocity and Sauter mean diameter data from Marchione *et al.* (2007) at 8, 10, 12, 14, 16, 18, and 20 mm downstream.

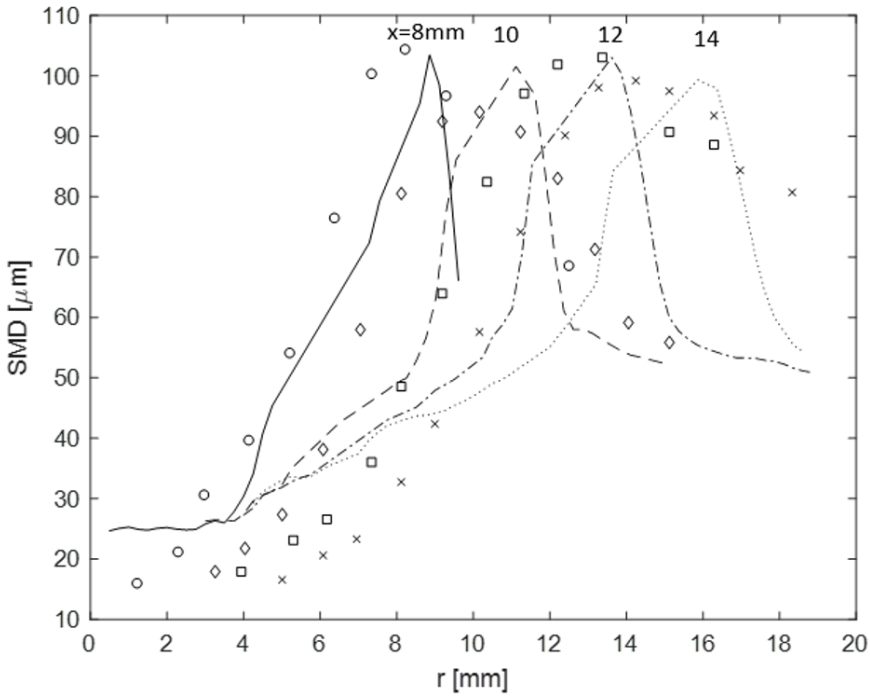

Figure 7.5: Computed SMD radial distributions compared to experimental data for measurement planes at 8, 10, 12, and 14 mm downstream. The data is from Marchione *et al.* (2007).

The drop size is fairly well reproduced as shown in Figure 7.5 and Figure 7.6. However, the profiles (the radial distributions of the droplets) are further out in the radial direction than the measurements up to x = 14 mm. This apparently has to do with the initial velocity vector, and since the liquid sheet is curved in swirl sprays any deviations in the initial velocity vector will lead to spread in the drop size profiles. Beyond x=14 mm, the trajectories of the droplets agree reasonably well, and this is due to re-alignment of the velocity vectors for the droplets injected at the furthest point of x = 5 mm. This points to the need for fine-tuning of the injection location to apply Equation (3.3) in this type of simulation. For the droplet velocity, there is a decent agreement for the peak velocity magnitude and locations, although similar deviations in the width of the velocity profiles are observed.

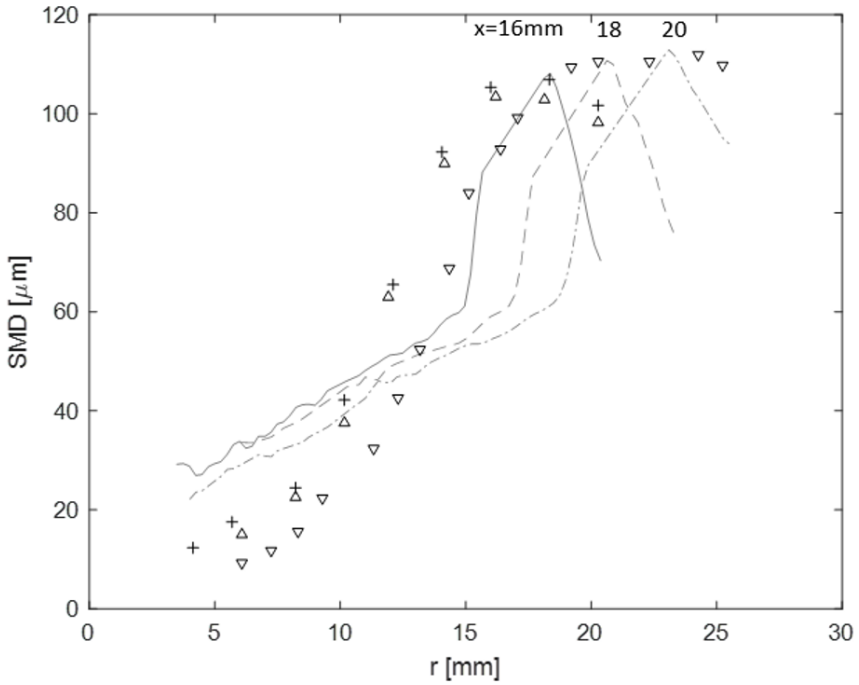

Figure 7.6: Computed SMD radial distributions compared to experimental data for measurement planes at 16, 18, and 20 mm downstream. The data is from Marchione *et al.* (2007).

Also, in the simulations very low droplet velocities appear in the periphery of the spray, whereas the minimum measured drop velocities are 5 to 6 m/s in Figures 7.7 and 7.8.

Again, the spray shape for swirl injection can be visualized by contour-plotting the number density of the droplets, in Figure 7.9. The lobes in the periphery of the spray are due to two factors: first, there is a similar lobe in the liquid velocity simulations (Figure 7.2) so that the mean motion may be following that path; and secondly, it is possible that discrete injection locations lead to such lobes, which can be remedied by increasing the increasing the number of injection planes.

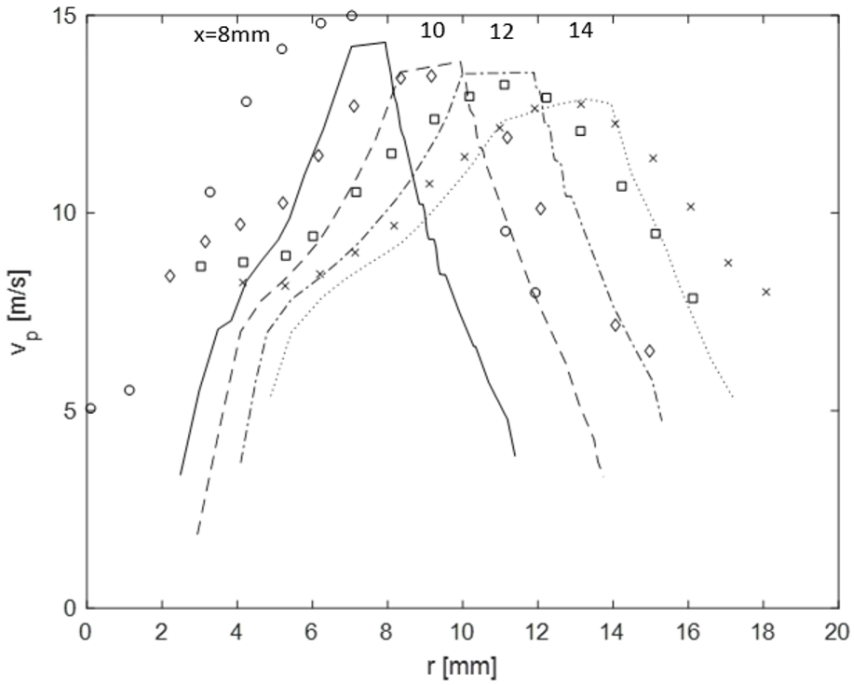

Figure 7.7: Computed particle velocity radial distributions compared to experimental data for measurement planes at 8, 10, 12, and 14 mm downstream. The data is from Marchione *et al.* (2007).

Global drop size distribution can also be sampled from the simulation, at x = 20 mm for example across the spray plane, as shown in Figure 7.10. Drop size distributions were not available from the measurements (Marchione *et al.* (2007)), and this could not be directly compared; however, the distribution shows a typical log-normal shape.

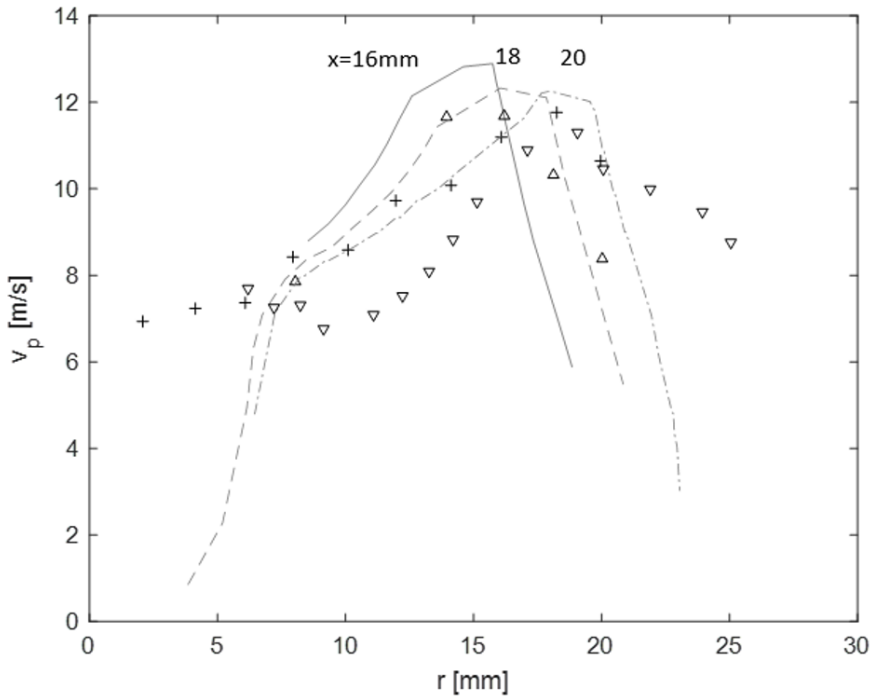

Figure 7.8: Computed particle velocity radial distributions compared to experimental data for measurement planes at 16, 18, and 20 mm downstream. The data is from Marchione *et al.* (2007).

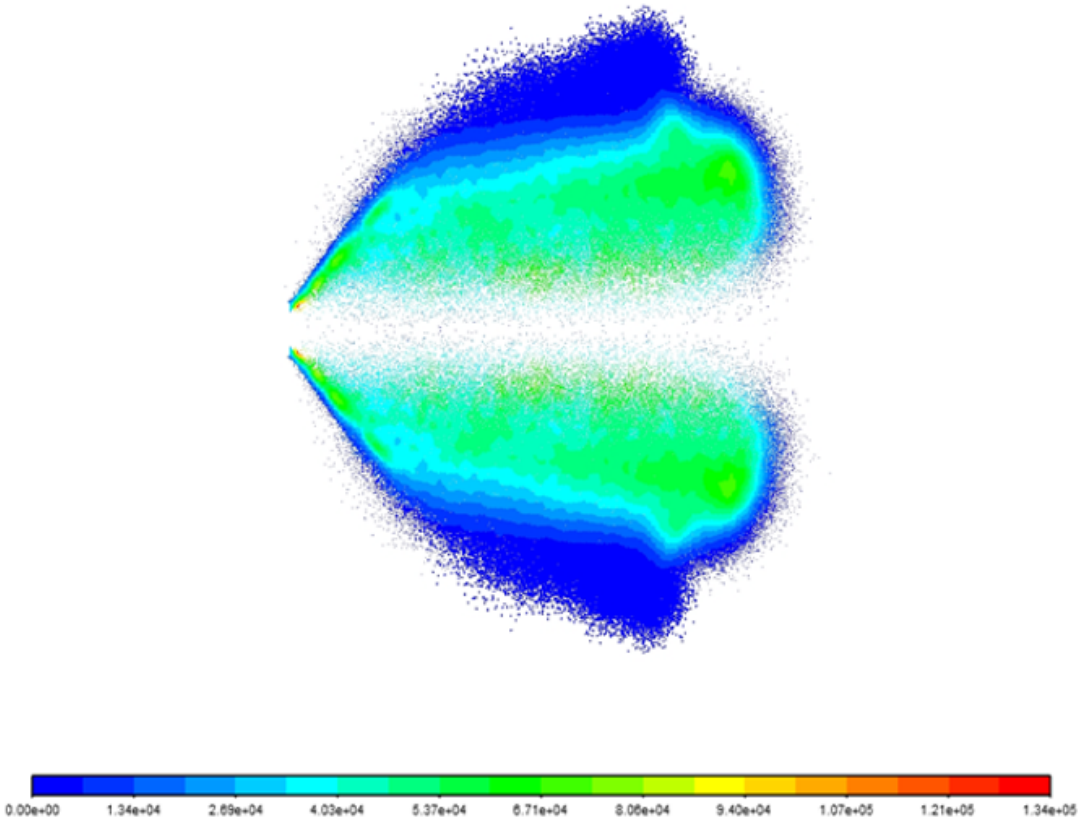

Figure 7.9: Particle tracks colored by number density for swirling spray.

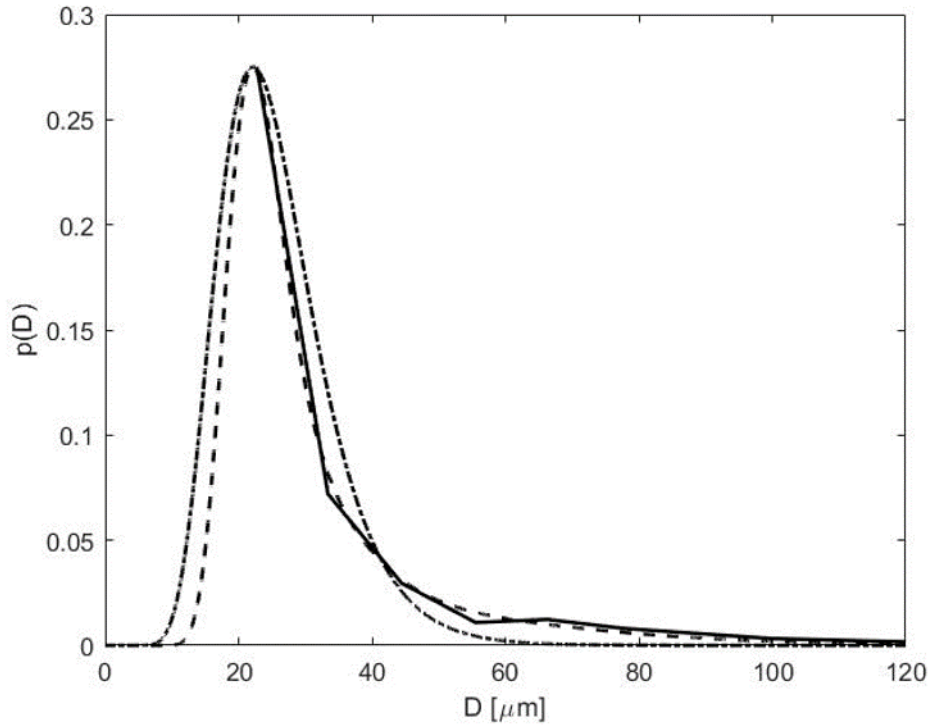

Figure 7.10: Global drop size distribution, $p(D)$, obtained at x=20 mm for swirling spray. The solid line is the sampled $p(D)$ from simulations, while the other lines are log-normal (dot-dashed) and curve (dashed) fits to the raw $p(D)$.

Chapter 8

CONCLUSIONS

From previous work by Lee and Robinson (2010) and Lee and An (2016), integral formulation of the conservation principles leads to the "quadratic formula" for determination of the drop size, in various spray geometries, which can also be useful as a generalized primary atomization module in computational simulations of spray flows. This quadratic formula is adopted within computational framework to simulate the full spray flow. The resulting computational protocol consists of (1) continuous liquid simulation, (2) atomization, and (3) dispersed droplet trajectory calculations. The atomization component is the quadratic formula. From examination of the results including comparison with experimental data, it appears that this computational protocol works quite well for pressure-atomized sprays with and without swirl. The protocol is easy to implement, computationally efficient, and robust in producing realistic spray flow simulations including the drop size, velocity and spray contours. For straight (no swirl) injection, physical atomization criterion is easy to define, leading to convincing results. For swirl sprays, a different atomization criterion is needed, to reflect different spray shape and geometry. The selection of the atomization criterion (and therefore location) along with adaptations to other spray geometries, such as liquid jets in cross flows and air-blast atomization, are the areas where further work is needed. Additionally, this protocol can be numerically implemented into preexisting codes in the form of coded algorithms. The primary outcome of this work is the convincing evidence of the estimation power of the quadratic formula and ease of implementation of the outlined protocol to existing CFD solvers.

REFERENCES

Beale, J. C. and R. D. Reitz, "Modeling spray atomization with the kelvin-helmholtz/rayleigh-taylor hybrid model", Atomization and sprays **9**, 6 (1999).

Chhetri, A. and K. Watts, "Surface tensions of petro-diesel, canola, jatropha and soapnut biodiesel fuels at elevated temperatures and pressures", Fuel **104**, 704–710 (2013).

EngineeringToolBox, "Liquids-kinematic viscosities", `https://www.engineeringtoolbox.com/kinematic-viscosity-d_397.html` (2003).

Fluent, "Ansys fluent theory guide", ANSYS Inc., USA **15317**, 724–746 (2011).

Lee, C. S. and S. W. Park, "An experimental and numerical study on fuel atomization characteristics of high-pressure diesel injection sprays", Fuel **81**, 18, 2417–2423 (2002).

Lee, T.-W. and K. An, "Quadratic formula for determining the drop size in pressure-atomized sprays with and without swirl", Physics of Fluids **28**, 6, 063302 (2016).

Lee, T.-W. and D. Robinson, "Calculation of the drop size distribution and velocities from the integral form of the conservation equations", Combustion Science and Technology **183**, 3, 271–284 (2010).

Marchione, T., C. Allouis, A. Amoresano and F. Beretta, "Experimental investigation of a pressure swirl atomizer spray", Journal of Propulsion and Power **23**, 5, 1096–1101 (2007).

Martinez, G. L., G. M. Magnotti, B. W. Knox, C. L. Genzale, K. E. Matusik, D. J. Duke, C. F. Powell and A. L. Kastengren, "Quantification of sauter mean diameter in diesel sprays using scattering-absorption extinction measurements", Tech. rep., Georgia Tech Research Corp. (2017).

Qin, L.-z., R. Yi and L.-j. Yang, "Theoretical breakup model in the planar liquid sheets exposed to high-speed gas and droplet size prediction", International Journal of Multiphase Flow **98**, 158–167 (2018).

Ruff, G., L. Bernal and G. Faeth, "Structure of the near-injector region of nonevaporating pressure-atomized sprays", Journal of Propulsion and Power **7**, 2, 221–230 (1991).

Saeedipour, M., S. Pirker, S. Bozorgi and S. Schneiderbauer, "An eulerian–lagrangian hybrid model for the coarse-grid simulation of turbulent liquid jet breakup", International Journal of Multiphase Flow **82**, 17–26 (2016).

APPENDIX A

STRAIGHT AND SWIRLING JETS QUADRATIC FORMULA MATLAB CODE

```
u=;     % Velocity from VOF simulation
sig=;     % Surface tension
K=;   % Viscous dissipation parameter used in quad. form., K'
rho=;   % Liquid density
ui=; % Injector inlet velocity
mu1=; % Liquid Viscosity
D32=[3*sig+sqrt(9*sig^2+(K*rho*mu1.*u.^2.*(ui^2-u.^2))./(2))] . . .
        ./[rho*(ui^2-u.^2)/2]
  %   Quadratic Formula. Returns values in meters
```

APPENDIX B

NUMBER FLOW RATE MATLAB CODE

```
d32m=; % SMD from quad. form. in microns
md=; % Mass flow rate
Vd=pi/6*(d32m*10^(-6))^3; % Volume of the SMD
rho=; % Density
N=md/(Vd*rho) % Number flow rate is particles per second
```

APPENDIX C

USER DEFINED MEMORY CODE

```
#include "udf.h"
#include "surf.h"
#include "dpm.h"

static int counter=0;

DEFINE_ADJUST(adjust_spray, d){
Thread *t;
cell_t c;

if (counter==0)
{counter=1;
thread_loop_c (t,d)
{
begin_c_loop (c,t)
{
C_UDMI(c,t,0)=0.0;

C_UDMI(c,t,1)=0.0;
C_UDMI(c,t,2)=0.0;
C_UDMI(c,t,3)=0.0;
C_UDMI(c,t,4)=0.0;
C_UDMI(c,t,5)=0.0; }
end_c_loop (c,t) }
}

thread_loop_c (t,d)
{
begin_c_loop (c,t)
{
C_UDMI(c,t,6) = C_UDMI(c,t,1)/MAX(C_UDMI(c,t,0),DPM_SMALL);
C_UDMI(c,t,7) = sqrt(C_UDMI(c,t,2)/MAX(C_UDMI(c,t,0),DPM_SMALL));
C_UDMI(c,t,8) = pow(C_UDMI(c,t,3) . . .
                    /MAX(C_UDMI(c,t,0),DPM_SMALL),0.333333);
C_UDMI(c,t,9) = C_UDMI(c,t,3)/MAX(C_UDMI(c,t,2),DPM_SMALL);
}
end_c_loop (c,t)
}
}

DEFINE_DPM_BODY_FORCE(body_force_spray, p, i)
{
Thread *t;
cell_t c;
real num_p, dia;
```

```
c = P_CELL(p);
t = P_CELL_THREAD(p);
if(P_USER_REAL(p,0) != (float) c)
{num_p = p->number_in_parcel;
dia = p->state.diam;
C_UDMI(c,t,0) += num_p;
C_UDMI(c,t,1) += num_p * dia;
C_UDMI(c,t,2) += num_p * dia * dia; C_UDMI(c,t,3)
+= num_p * dia * dia * dia; C_UDMI(c,t,4) +=
num_p * dia * dia * dia * dia; C_UDMI(c,t,5) += 1;
P_USER_REAL(p,0)=(float) c;}

return 0.0;
}
```

APPENDIX D

WATER JET VOF VELOCITY PROFILES

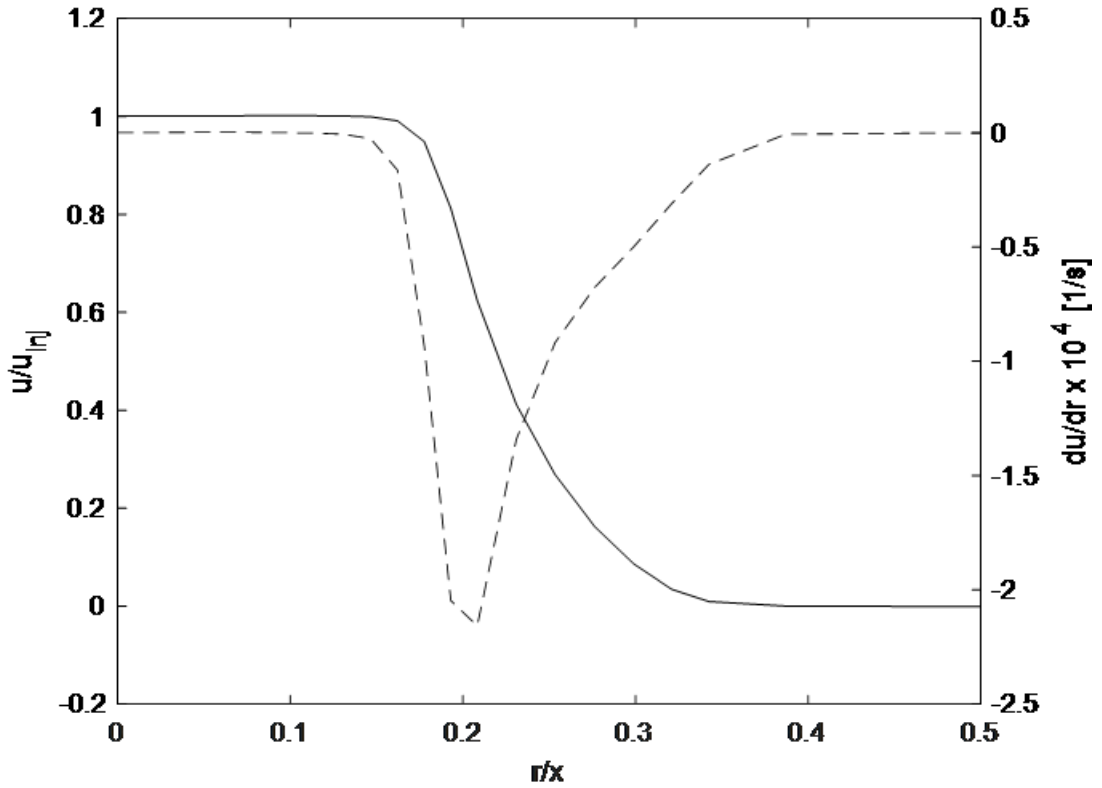

Figure D.1: Computed normalized axial velocity (solid line) and radial derivative of the axial velocity (dashed line) as a function of normalized radial distance taken at 5 diameters downstream of the injector.

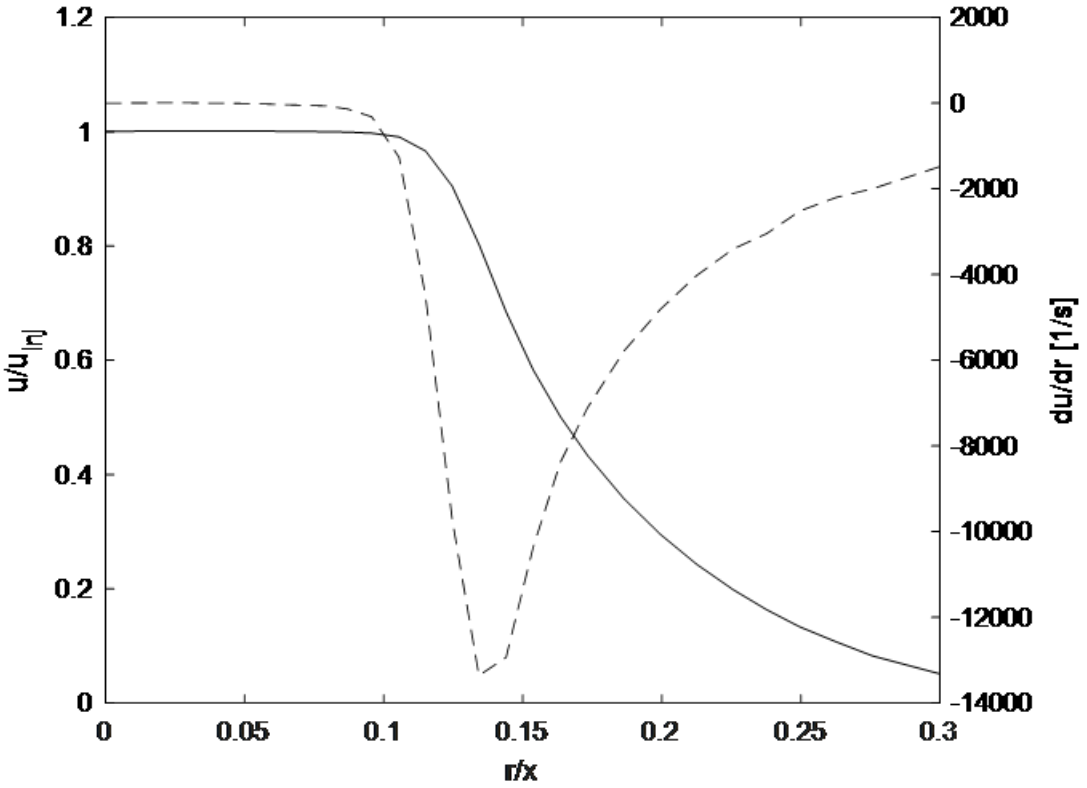

Figure D.2: Computed normalized axial velocity (solid line) and radial derivative of the axial velocity (dashed line) as a function of normalized radial distance taken at 10 diameters downstream of the injector.

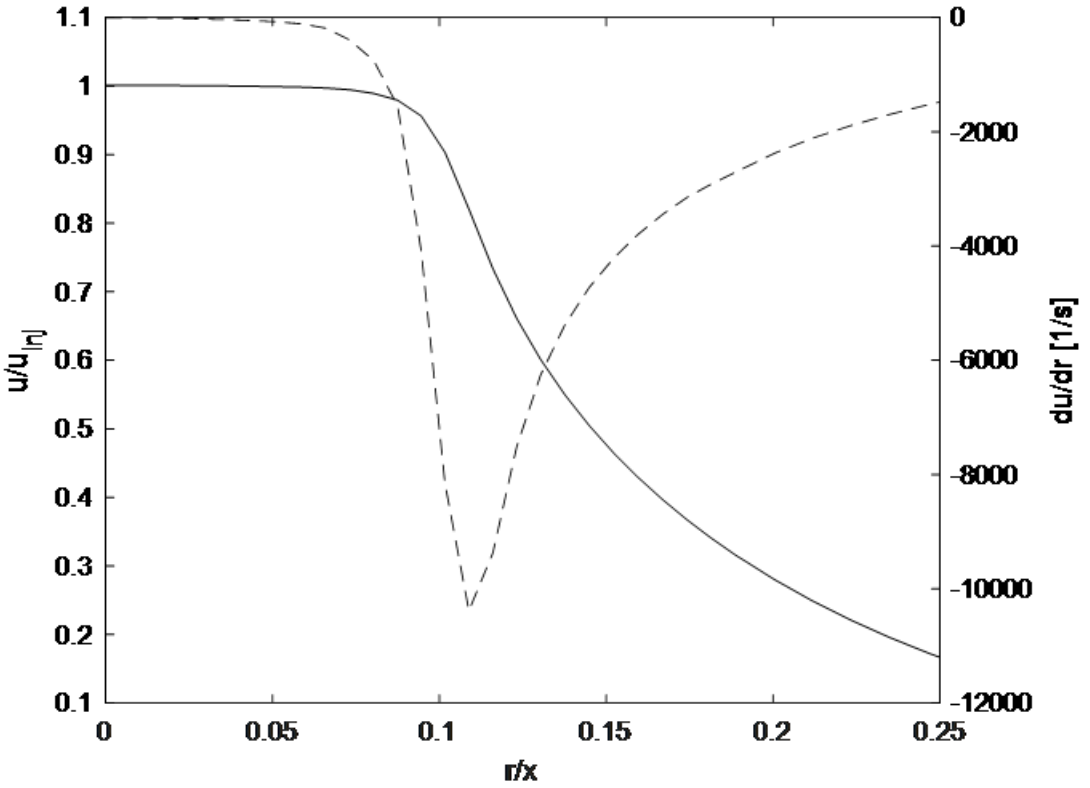

Figure D.3: Computed normalized axial velocity (solid line) and radial derivative of the axial velocity (dashed line) as a function of normalized radial distance taken at 20 diameters downstream of the injector.

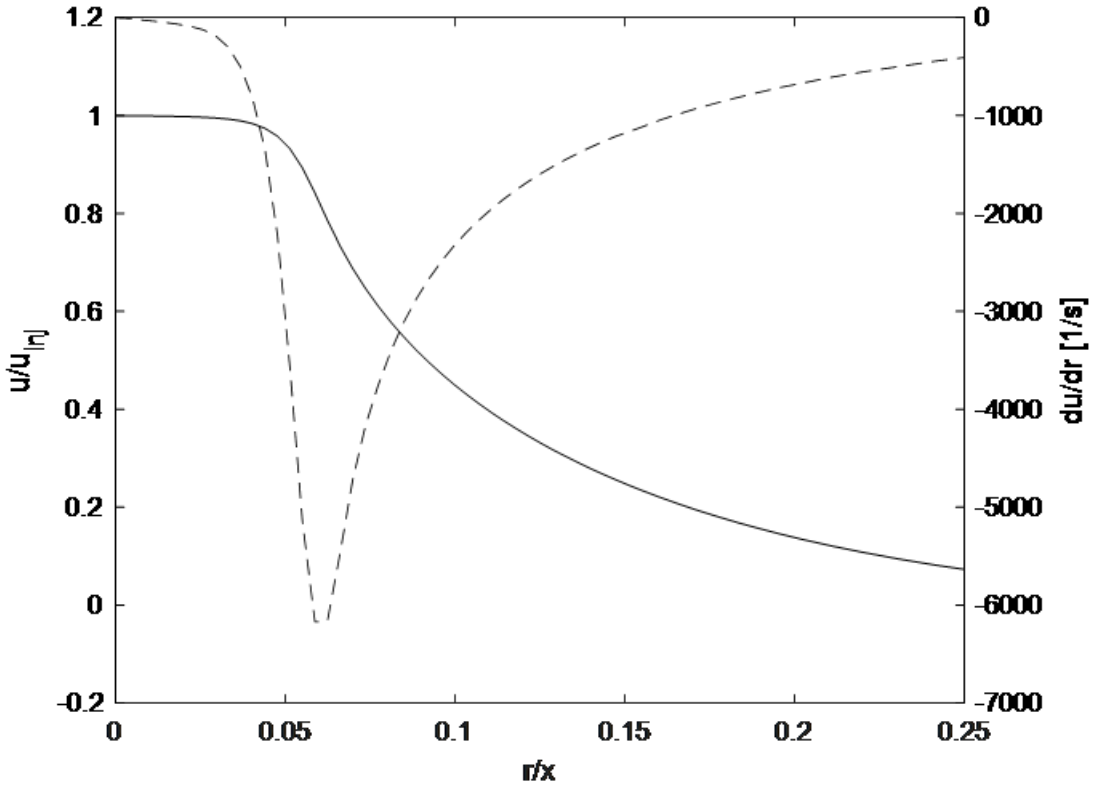

Figure D.4: Computed normalized axial velocity (solid line) and radial derivative of the axial velocity (dashed line) as a function of normalized radial distance taken at 40 diameters downstream of the injector.

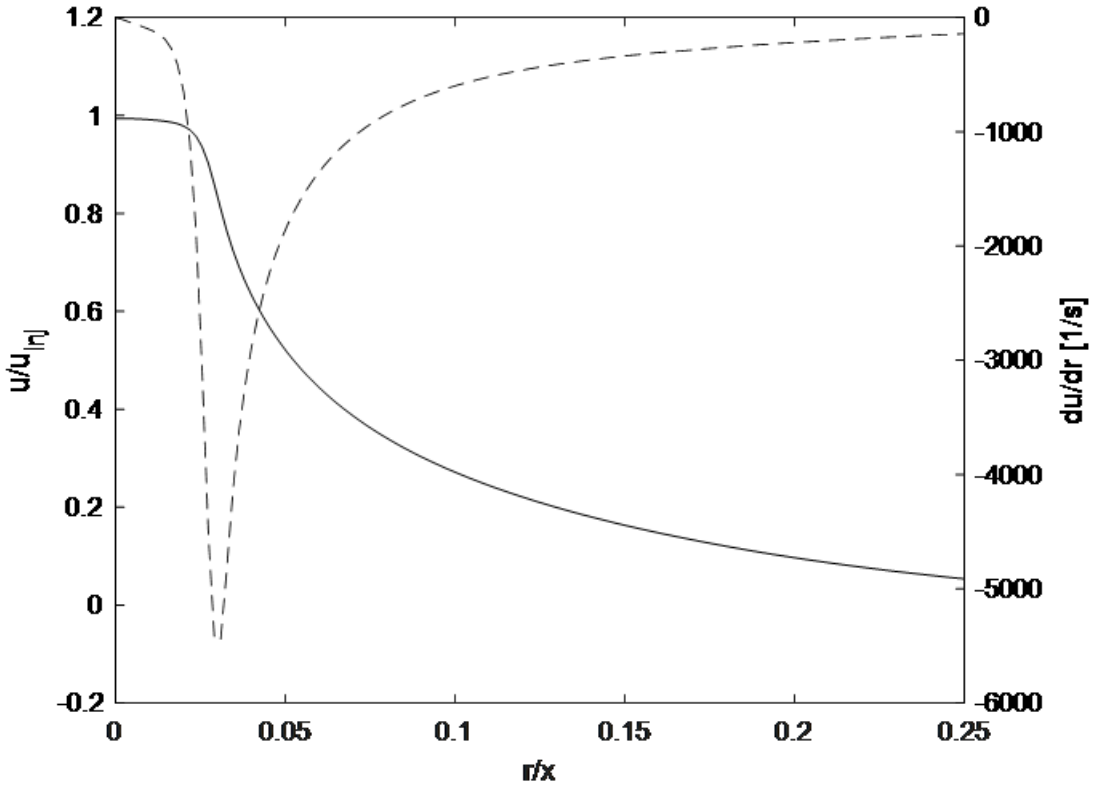

Figure D.5: Computed normalized axial velocity (solid line) and radial derivative of the axial velocity (dashed line) as a function of normalized radial distance taken at 80 diameters downstream of the injector.

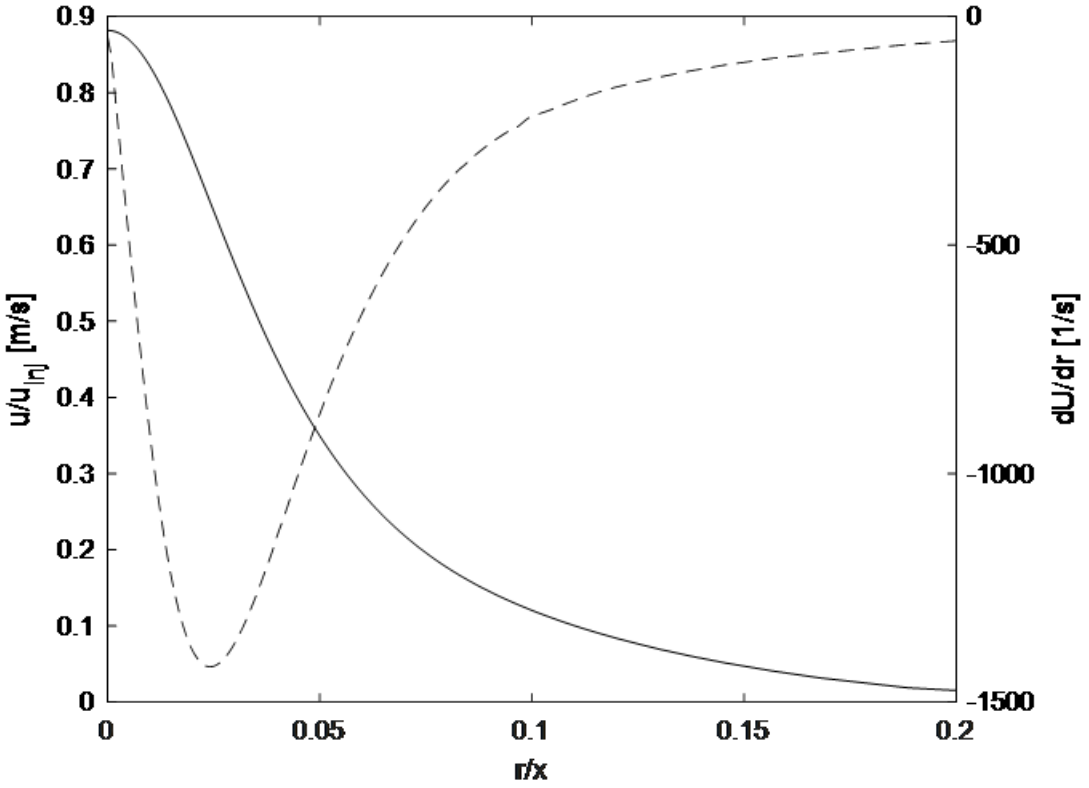

Figure D.6: Computed normalized axial velocity (solid line) and radial derivative of the axial velocity (dashed line) as a function of normalized radial distance taken at 104 diameters downstream of the injector. This velocity and derivative profile corresponds to the break-up location.

APPENDIX E

WATER JET INJECTION TABLES

$y[mm]$	$u[m/s]$	$v[m/s]$	$D_{32}[\mu m]$	$\dot{m}[kg/s]$	$n[1/s]$
0	49.9	0	837.0	0.9916	3.24e6
14.02	44.8	0.41	577.4	0.8887	8.83e6
21.9	38.82	0.595	420.8	0.7700	1.98e7
37.55	26.76	0.75	239.8	0.5308	7.37e7
53.01	18.09	0.84	150.9	0.3588	1.99e8

Table E.1: Tabulated point injection values for break-up point atomization at 104 diameters downstream.

$y[mm]$	$u[m/s]$	$v[m/s]$	$D_{32}[\mu m]$	$\dot{m}[kg/s]$	$n[1/s]$
8.73	53.8	0.0456	1346.8	0.022757	1.78e4
9.48	46.1	0.583	624.4	0.01948	1.53e5
10.24	35.4	0.81	358.0	0.01497	6.24e5
11.35	23.35	1.98	202.5	0.00988	2.28e6
12.45	15.2	2.85	124.7	0.00643	6.35e6

Table E.2: Tabulated point injection values for surface atomization at 5 diameters downstream.

$y[mm]$	$u[m/s]$	$v[m/s]$	$D_{32}[\mu m]$	$\dot{m}[kg/s]$	$n[1/s]$
10.93	54.8	0.158	1687.6	0.03037	1.21e4
12.75	45.5	0.351	602.0	0.02521	2.21e5
14.6	33.1	0.78	321.6	0.01832	1.05e6
16.46	24.6	1.15	215.4	0.01361	2.61e6
18.95	16.7	1.66	138.5	0.00928	6.68e6

Table E.3: Tabulated point injection values for surface atomization at 10 diameters downstream.

$y[mm]$	$u[m/s]$	$v[m/s]$	$D_{32}[\mu m]$	$\dot{m}[kg/s]$	$n[1/s]$
17.97	54.22	0.008	1465.1	0.02605	1.58e4
20.67	46.5	0.094	642.0	0.02233	1.62e5
23.41	37.5	0.290	394.4	0.01799	5.61e5
26.16	31.1	0.45	294.4	0.01496	1.12e6
28.92	26.4	0.62	235.1	0.01266	1.86e6

Table E.4: Tabulated point injection values for surface atomization at 20 diameters downstream.

$y[mm]$	$u[m/s]$	$v[m/s]$	$D_{32}[\mu m]$	$\dot{m}[kg/s]$	$n[1/s]$
19.5	52.85	0.012	1153.1	0.02512	3.14e4
22.31	47.7	0.015	698.1	0.02268	1.28e5
25.12	41.58	0.027	483.2	0.01976	3.35e5
27.95	36.68	0.047	380.0	0.01743	6.08e5
29.38	34.63	0.066	345.5	0.01646	7.64e5

Table E.5: Tabulated point injection values for surface atomization at 40 diameters downstream.

$y[mm]$	$u[m/s]$	$v[m/s]$	$D_{32}[\mu m]$	$\dot{m}[kg/s]$	$n[1/s]$
19.35	53.1	0.012	1191.3	0.02473	2.79e4
22.1	48.7	0.014	749.6	0.02268	1.03e5
24.86	43.4	0.0135	531.6	0.02021	2.57e5
26.24	41.1	0.015	471.8	0.01916	3.49e5
28.97	37.5	0.02	394.4	0.01746	7.83e5

Table E.6: Tabulated point injection values for surface atomization at 80 diameters downstream.

APPENDIX F

DIESEL ATOMIZATION VELOCITY PROFILES

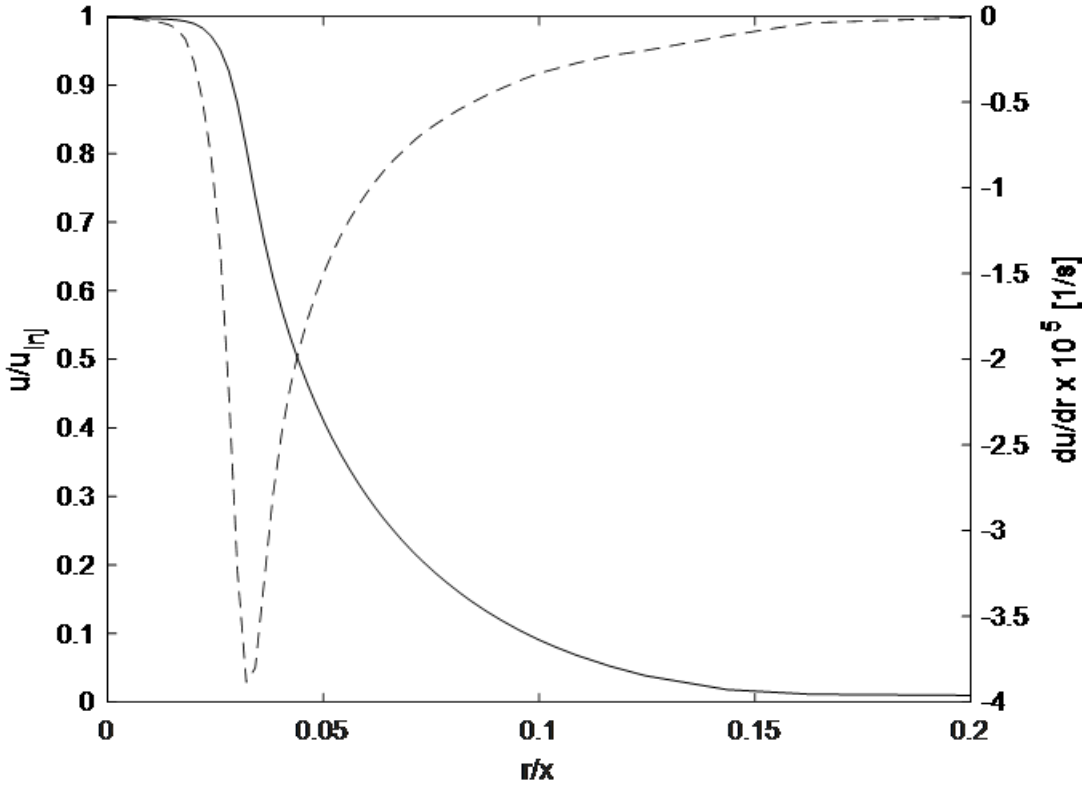

Figure F.1: Computed normalized axial velocity (solid line) and radial derivative of the axial velocity (dashed line) as a function of normalized radial distance taken at 5 mm downstream of the injector for Martinez et. al. (2017) validation case.

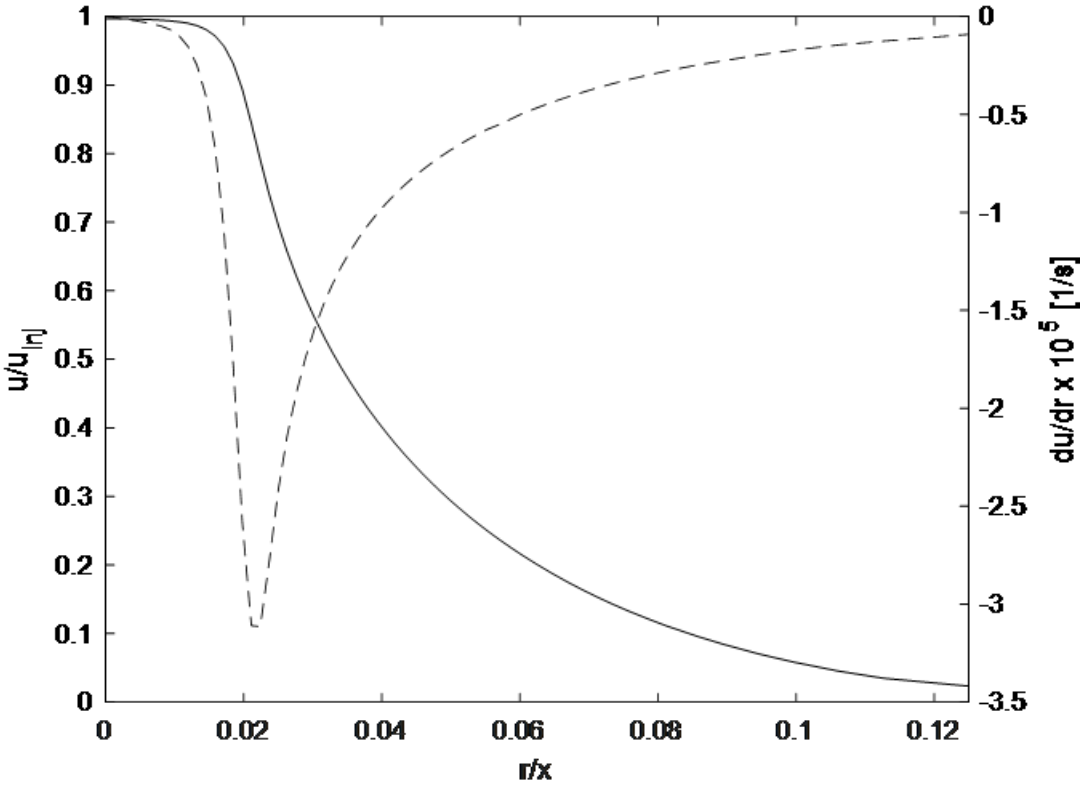

Figure F.2: Computed normalized axial velocity (solid line) and radial derivative of the axial velocity (dashed line) as a function of normalized radial distance taken at 7.5 mm downstream of the injector for Martinez et. al. (2017) validation case.

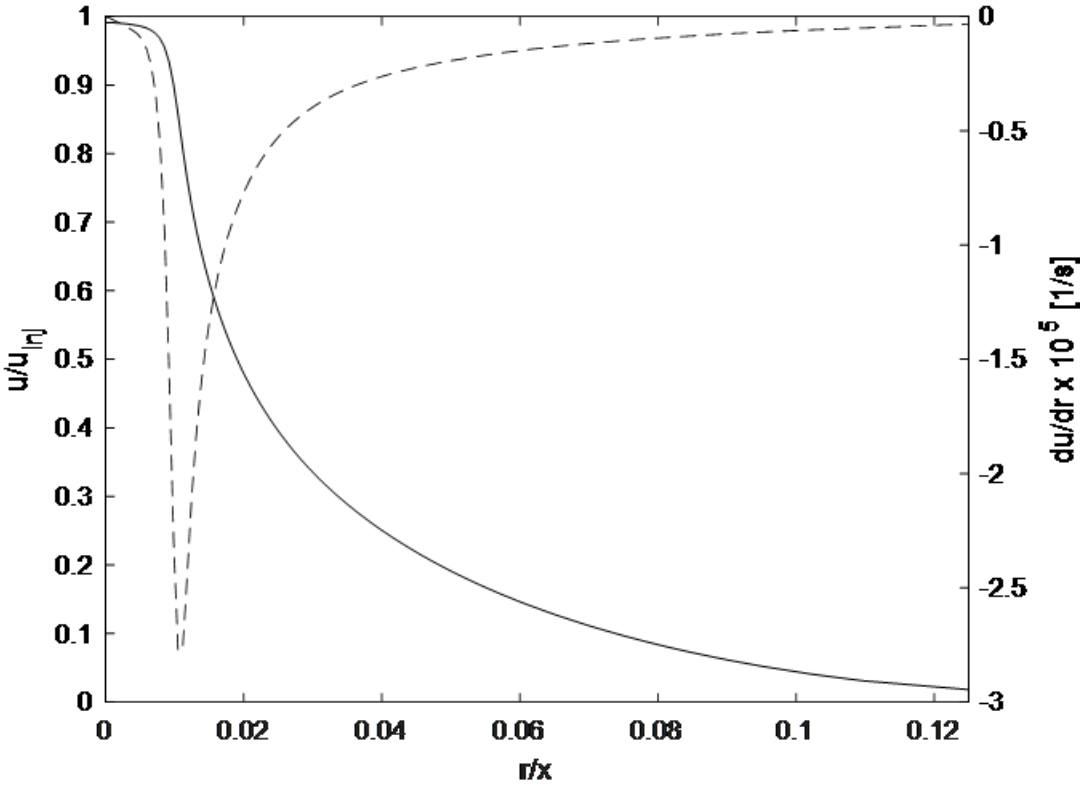

Figure F.3: Computed normalized axial velocity (solid line) and radial derivative of the axial velocity (dashed line) as a function of normalized radial distance taken at 15 mm downstream of the injector for Martinez et. al. (2017) validation case.

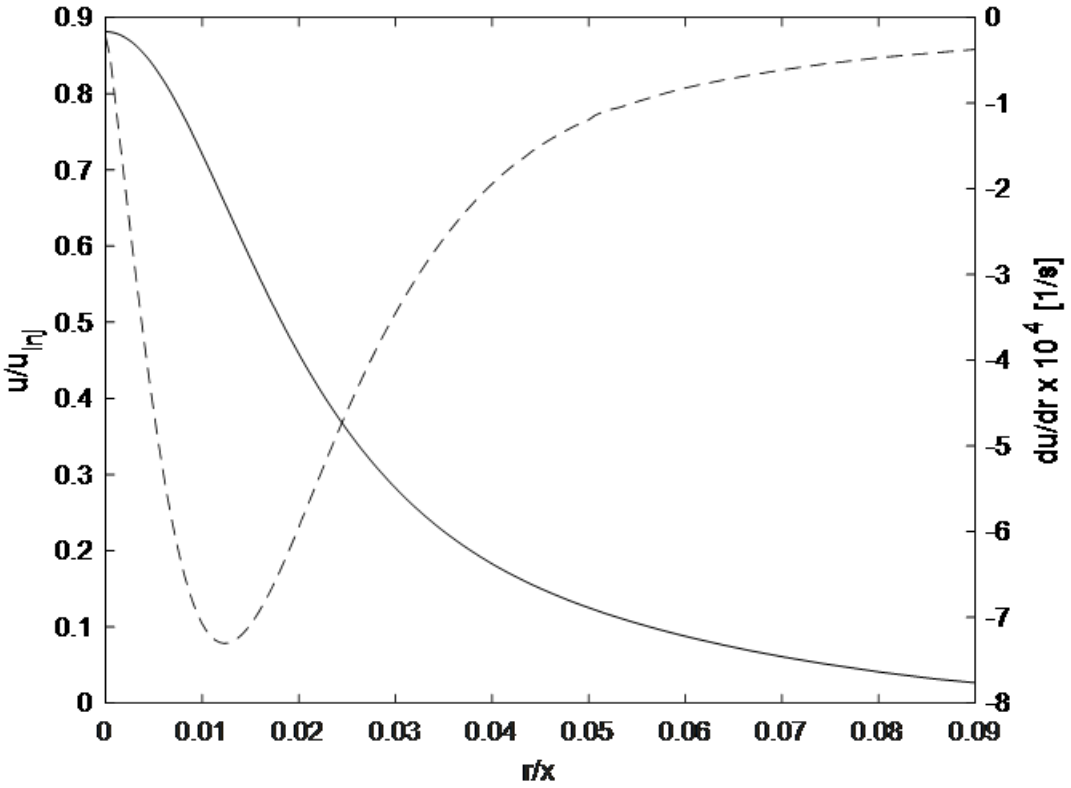

Figure F.4: Computed normalized axial velocity (solid line) and radial derivative of the axial velocity (dashed line) as a function of normalized radial distance taken at the break-up length, 21.6 mm downstream of the injector, for Martinez et. al. (2017) validation case.

APPENDIX G

DIESEL JET INJECTION TABLES: MARTINEZ ET. AL. VALIDATION CASE

$y[mm]$	$u[m/s]$	$v[m/s]$	$D_{32}[\mu m]$	$\dot{m}[kg/s]$	$n[1/s]$
0.1301	257	0.95	29.3	0.0001107	1.025e7
0.1504	235.6	1.15	16.8	0.0001015	4.98e7
0.1603	218.8	1.25	13.0	0.0000942	9.89e7
0.171	199.2	1.72	10.3	0.0000858	1.83e8
0.1814	181.7	2.2	8.6	0.0000783	2.87e8
0.2018	154.4	3.74	6.6	0.0000665	5.39e8
0.2215	134.0	4.51	4.9	0.0000577	1.14e9

Table G.1: Tabulated point injection values for surface atomization at 5 mm downstream.

$y[mm]$	$u[m/s]$	$v[m/s]$	$D_{32}[\mu m]$	$\dot{m}[kg/s]$
0.1386	251.5	1.39	24.1	0.0001067
0.1582	227.9	2.25	14.8	0.0000967
0.168	213.5	2.49	12.2	0.0000906
0.1777	199.9	2.74	10.4	0.0000848
0.1874	187.9	2.91	9.1	0.0000797
0.2069	167.9	3.24	7.5	0.0000712
0.2265	151.6	3.33	6.4	0.0000643

Table G.2: Tabulated point injection values for surface atomization at 7.5 mm downstream.

$y[mm]$	$u[m/s]$	$v[m/s]$	$D_{32}[\mu m]$	$\dot{m}[kg/s]$
0.1677	252.1	1.97	24.6	0.0000988
0.1775	243.2	2.37	19.6	0.0000953
0.1873	231.3	2.76	15.6	0.0000906
0.1971	218.4	2.78	12.9	0.0000856
0.2069	206.2	2.79	11.2	0.0000808
0.2265	186.5	2.82	9.0	0.0000731
0.2461	171.2	2.822	7.7	0.0000671

Table G.3: Tabulated point injection values for surface atomization at 15 mm downstream.

$y[mm]$	$u[m/s]$	$v[m/s]$	$D_{32}[\mu m]$	$\dot{m}[kg/s]$
0	238	0	17.6	0.0006907
0.05893	234.2	0.63	16.4	0.0006797
0.1275	221.1	1.367	13.5	0.0006417
0.1764	207.3	1.794	11.3	0.0006016
0.2156	194.6	2.084	9.8	0.0005647
0.2352	188.0	2.19	9.1	0.0005456
0.2646	177.8	2.35	8.2	0.0005159

Table G.4: Tabulated point injection values for break-up point atomization at 21.6 mm downstream.

APPENDIX H

DIESEL JET INJECTION TABLES: CHANG AND PARK VALIDATION CASE

$y[mm]$	$u[m/s]$	$v[m/s]$	$D_{32}[\mu m]$	$\dot{m}[kg/s]$	$n[1/s]$
0.2098	253.4	0.94	55.3	0.000176	2.42e6
0.2426	232.3	1.13	31.8	0.000161	1.17e7
0.2585	215.8	1.23	24.7	0.000150	2.32e7
0.2758	196.4	1.69	19.5	0.000136	4.27e7
0.2926	179.2	2.2	16.2	0.000124	6.79e7
0.3255	152.2	3.69	12.4	0.000106	1.29e8
0.3573	132.1	4.45	10.2	0.000092	2.01e8

Table H.1: Tabulated point injection values for surface atomization at 8 mm downstream.

$y[mm]$	$u[m/s]$	$v[m/s]$	$D_{32}[\mu m]$	$\dot{m}[kg/s]$
0.2235	247.9	1.38	45.5	0.000170
0.2552	224.7	2.22	28.0	0.000154
0.2709	210.5	2.46	23.0	0.000144
0.2866	197.1	2.70	19.6	0.000135
0.3023	185.3	2.87	17.3	0.000127
0.3337	165.6	3.20	14.1	0.000113
0.3653	149.5	3.28	12.1	0.000102

Table H.2: Tabulated point injection values for surface atomization at 12 mm downstream.

$y[mm]$	$u[m/s]$	$v[m/s]$	$D_{32}[\mu m]$	$\dot{m}[kg/s]$
0.2705	248.6	1.94	46.5	0.000157
0.2863	239.8	2.34	36.9	0.000152
0.3021	228.1	2.72	29.6	0.000144
0.3179	215.4	2.74	24.5	0.000136
0.3337	203.3	2.75	21.1	0.000129
0.3653	183.9	2.78	17.0	0.000116
0.3969	168.8	2.78	14.6	0.000107

Table H.3: Tabulated point injection values for surface atomization at 24 mm downstream.

$y[mm]$	$u[m/s]$	$v[m/s]$	$D_{32}[\mu m]$	$\dot{m}[kg/s]$
0	234.7	0	33.3	0.001099
0.0950	230.9	0.62	31.0	0.001081
0.2056	218.0	1.35	25.4	0.001021
0.2845	204.4	1.77	21.3	0.000957
0.3477	191.9	2.05	18.5	0.000898
0.3794	185.4	2.16	17.3	0.000868
0.4268	175.3	2.32	15.6	0.000821

Table H.4: Tabulated point injection values for break-up point atomization at 34.8 mm downstream.

APPENDIX I

SWIRLING SPRAY ATOMIZATION VELOCITY PROFILES

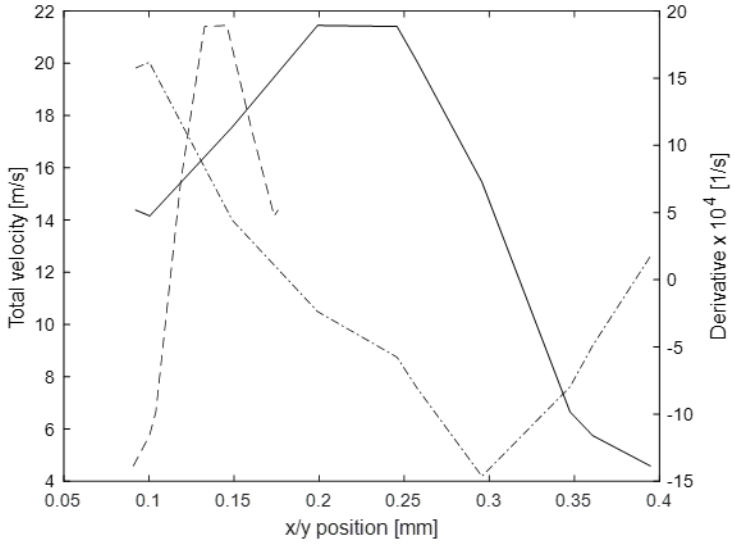

Figure I.1: Computed velocity magnitude versus y-coordinate (solid line), velocity magnitude versus x-coordinate (dashed line), and total derivative versus y-coordinate (dot-dashed line) at x=0.146 mm downstream.

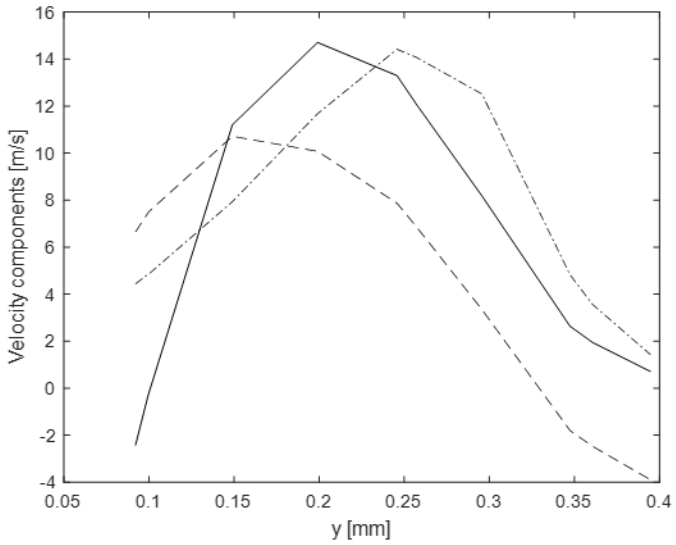

Figure I.2: Computed axial velocity (solid line), radial velocity (dashed line), and tangential velocity (dot-dashed line) versus y-coordinate at x=0.146 mm downstream.

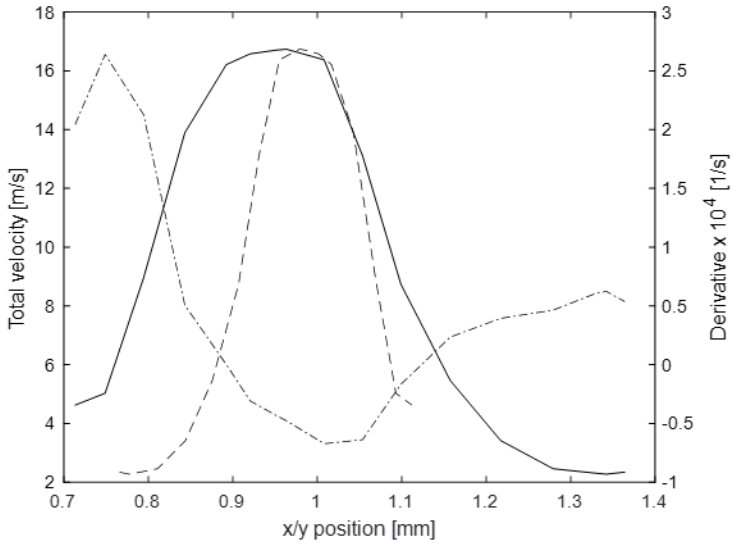

Figure I.3: Computed velocity magnitude versus y-coordinate (solid line), velocity magnitude versus x-coordinate (dashed line), and total derivative versus y-coordinate (dot-dashed line) at x=1 mm downstream.

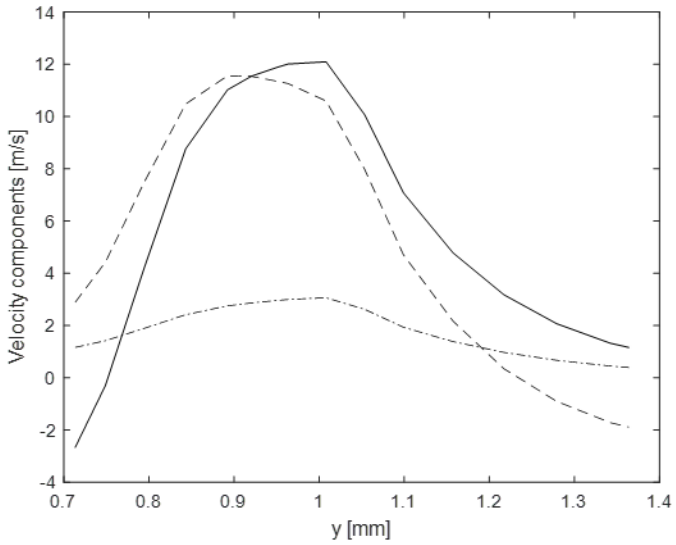

Figure I.4: Computed axial velocity (solid line), radial velocity (dashed line), and tangential velocity (dot-dashed line) versus y-coordinate at x=1 mm downstream.

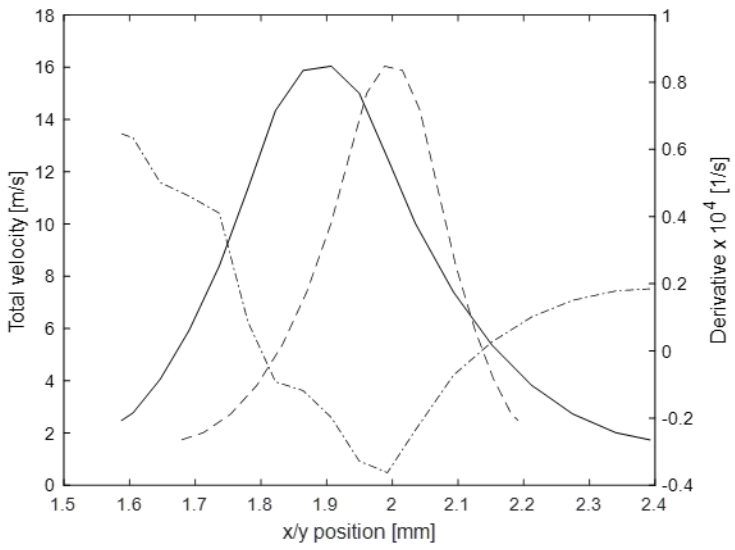

Figure I.5: Computed velocity magnitude versus y-coordinate (solid line), velocity magnitude versus x-coordinate (dashed line), and total derivative versus y-coordinate (dot-dashed line) at x=2 mm downstream.

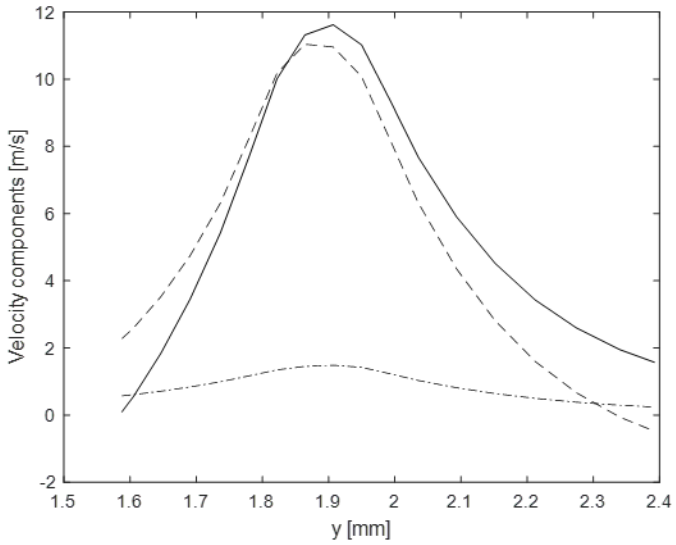

Figure I.6: Computed axial velocity (solid line), radial velocity (dashed line), and tangential velocity (dot-dashed line) versus y-coordinate at x=2 mm downstream.

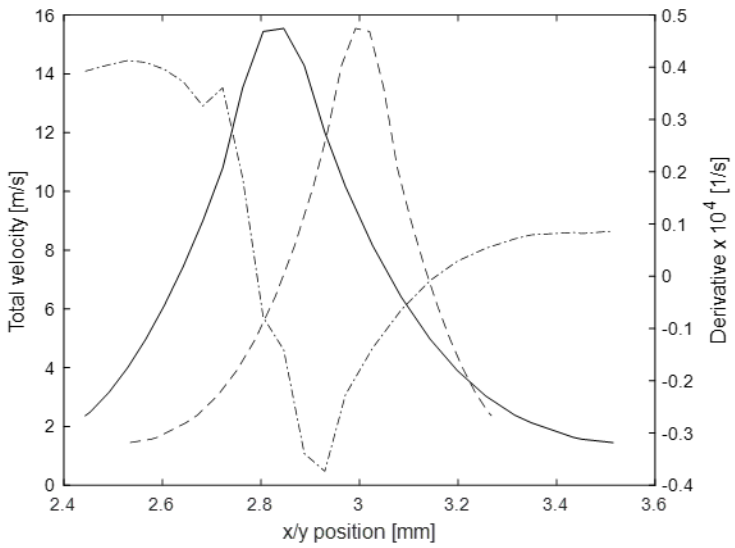

Figure I.7: Computed velocity magnitude versus y-coordinate (solid line), velocity magnitude versus x-coordinate (dashed line), and total derivative versus y-coordinate (dot-dashed line) at x=3 mm downstream.

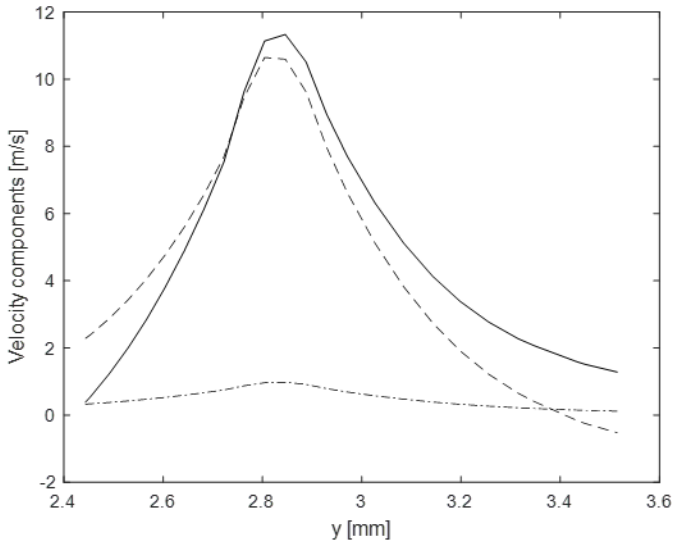

Figure I.8: Computed axial velocity (solid line), radial velocity (dashed line), and tangential velocity (dot-dashed line) versus y-coordinate at x=3 mm downstream.

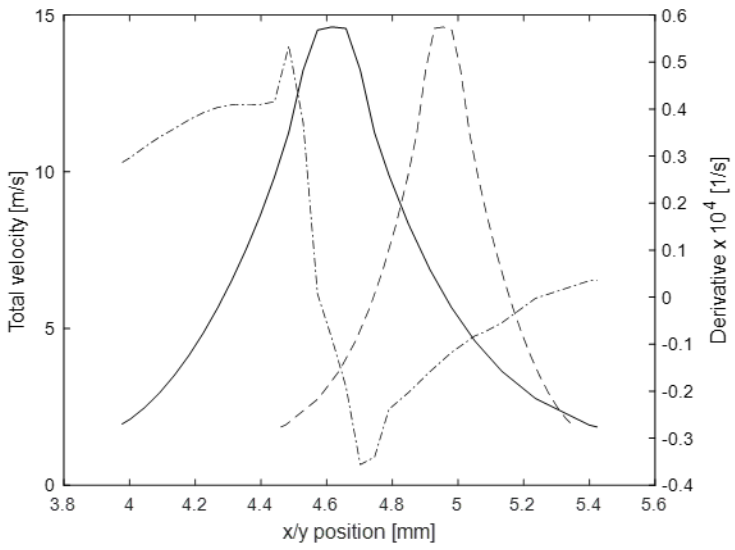

Figure I.9: Computed velocity magnitude versus y-coordinate (solid line), velocity magnitude versus x-coordinate (dashed line), and total derivative versus y-coordinate (dot-dashed line) at x=5 mm downstream.

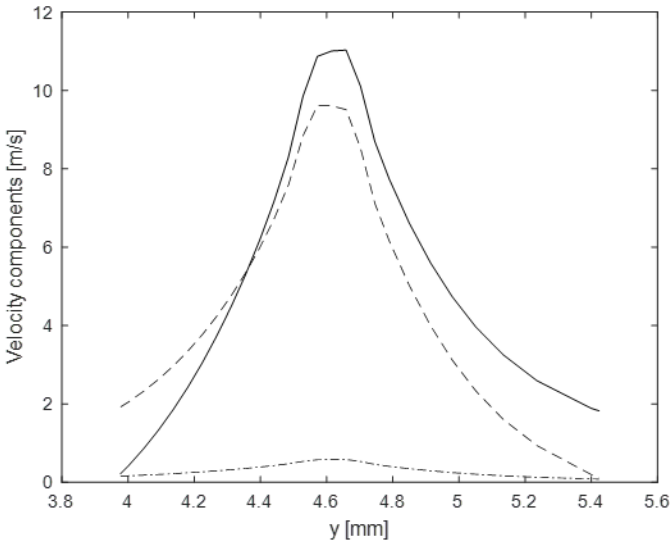

Figure I.10: Computed axial velocity (solid line), radial velocity (dashed line), and tangential velocity (dot-dashed line) versus y-coordinate at x=5 mm downstream.

APPENDIX J

SWIRLING SPRAY INJECTION TABLES

$y[mm]$	$x[mm]$	$\overline{u}[m/s]$	$D_{32}[\mu m]$	$u[m/s]$	$v[m/s]$	$w[m/s]$	$\dot{m}[kg/s]$	$n[1/s]$
0.0995	0.1738	14.18	54.8	3	7.5	4.8	0.007601	1.077e8
0.1490	0.1599	17.57	77.8	11.2	10.7	7.9	0.00943	7.662e7
0.1991	0.1458	21.45	127.4	14.7	10.1	11.7	0.01151	1.269e7
0.2457	0.1327	21.41	126.6	13.3	7.9	14.4	0.01148	1.319e7
0.2572	0.1294	20.1	104.9	12.1	6.9	14.1	0.01078	2.216e7
0.2956	0.1186	15.46	62.4	8.2	3.3	12.5	0.00829	7.950e7

Table J.1: Tabulated point injection values for 0.146 mm downstream.

$y[mm]$	$x[mm]$	$\overline{u}[m/s]$	$D_{32}[\mu m]$	$u[m/s]$	$v[m/s]$	$w[m/s]$	$\dot{m}[kg/s]$
0.7488	1.093	5.0	16.7	2.9	4.4	1.4	0.003003
0.7943	1.069	8.9	30.8	4.2	7.5	1.9	0.005342
0.8432	1.043	13.9	53.2	8.8	10.5	2.4	0.008296
0.8923	1.017	16.2	67.4	11.0	11.6	2.7	0.009682
0.9634	0.9789	16.7	71.2	12.0	11.3	2.9	0.009998
1.008	0.9551	16.4	68.5	12.1	10.6	3.1	0.009778

Table J.2: Tabulated point injection values for 1 mm downstream.

$y[mm]$	$x[mm]$	$\overline{u}[m/s]$	$D_{32}[\mu m]$	$u[m/s]$	$v[m/s]$	$w[m/s]$	$\dot{m}[kg/s]$
1.737	2.097	8.4	28.7	5.4	6.3	0.9	0.00478
1.780	2.069	11.4	40.8	7.7	8.3	1.2	0.00646
1.822	2.042	14.3	55.7	10.0	10.2	1.3	0.00816
1.907	1.988	16.0	66.2	11.6	10.9	1.5	0.00913
1.950	1.961	15.0	59.6	11.0	10.1	1.4	0.00854
1.992	1.934	12.5	46.3	9.4	8.2	1.2	0.00713

Table J.3: Tabulated point injection values for 2 mm downstream.

$y[mm]$	$x[mm]$	$\overline{u}[m/s]$	$D_{32}[\mu m]$	$u[m/s]$	$v[m/s]$	$w[m/s]$	$\dot{m}[kg/s]$
2.722	3.077	10.8	38.3	7.5	7.7	0.7	0.00566
2.763	3.049	13.5	51.3	9.6	9.5	0.9	0.00710
2.804	3.021	15.4	62.3	11.1	10.7	0.9	0.00809
2.846	2.992	15.5	62.9	11.3	10.6	0.9	0.00815
2.888	2.963	14.3	55.4	10.5	9.6	0.9	0.00749
2.930	2.935	12.0	43.7	8.9	7.9	0.8	0.00629

Table J.4: Tabulated point injection values for 3 mm downstream.

$y[mm]$	$x[mm]$	$\overline{u}[m/s]$	$D_{32}[\mu m]$	$u[m/s]$	$v[m/s]$	$w[m/s]$	$\dot{m}[kg/s]$
4.485	5.034	11.3	40.4	8.3	7.6	0.5	0.00556
4.528	5.008	13.2	49.8	9.8	8.8	0.5	0.00654
4.572	4.981	14.5	56.7	10.9	9.6	0.6	0.00717
4.611	4.957	14.6	57.3	10.9	9.6	0.6	0.00721
4.659	4.928	14.57	57.0	11.0	9.5	0.6	0.00719
4.702	4.901	13.2	49.8	10.1	8.5	0.5	0.00654

Table J.5: Tabulated point injection values for 5 mm downstream.